

<sup>1</sup> **Upper Limits on Perturbations of Nuclear Decay Rates  
2                          Induced by Reactor Electron Antineutrinos**

<sup>3</sup>                          V.E. Barnes,<sup>1,2</sup> D.J. Bernstein,<sup>1</sup> C.D. Bryan,<sup>3</sup> N. Cinko,<sup>1</sup>  
<sup>4</sup>                          G.G. Deichert,<sup>3</sup> J.T. Gruenwald,<sup>1,2</sup> J.M. Heim,<sup>1</sup> H.B. Kaplan,<sup>1</sup>  
<sup>5</sup>                          R. LaZur,<sup>1</sup> D. Neff,<sup>1</sup> J.M. Nistor,<sup>1</sup> N. Sahelijo,<sup>1</sup> and E. Fischbach<sup>1,2,\*</sup>

<sup>6</sup>                          <sup>1</sup>*Department of Physics & Astronomy,*  
<sup>7</sup>                          *Purdue University, West Lafayette, IN 47907 U.S.A.*

<sup>8</sup>                          <sup>2</sup>*SNARE Inc., West Lafayette, IN 47906 U.S.A.*

<sup>9</sup>                          <sup>3</sup>*High Flux Isotope Reactor (HFIR),*  
<sup>10</sup>                        *Oak Ridge National Laboratory, P.O. Box 2008, Oak Ridge, TN 37831 U.S.A.*

<sup>11</sup>                        (Dated: January 15, 2020)

## Abstract

We report the results of an experiment conducted near the High Flux Isotope Reactor of Oak Ridge National Laboratory, designed to address the question of whether a flux of reactor-generated electron antineutrinos ( $\bar{\nu}_e$ ) can alter the rates of weak nuclear interaction induced decays of  $^{54}\text{Mn}$ ,  $^{22}\text{Na}$ , and  $^{60}\text{Co}$ . This experiment has small statistical errors but, when systematic uncertainties are included, has null results. Perturbations greater than one part in  $10^4$  are excluded at 95% confidence level in  $\beta^\pm$  decay and electron capture processes, in the presence of an antineutrino flux of  $3 \times 10^{12} \text{ cm}^{-2}\text{s}^{-1}$ . The present experimental methods are applicable to a wide range of radionuclides. Improved sensitivity in future experiments can be anticipated as we continue to better understand and reduce the dominant systematic uncertainties.

**Keywords:** Reactor Physics, Neutrino Physics

---

\* Corresponding Author: ephraim@purdue.edu

<sup>12</sup> **I. INTRODUCTION**

<sup>13</sup> Few issues frame the history of natural radioactivity as fundamentally as the question  
<sup>14</sup> of whether radioactive decays are affected by their local environment. There is evidence to  
<sup>15</sup> support this suggestion, including recent studies which have reported evidence of a solar  
<sup>16</sup> influence on certain radioactive decay processes. This includes annual oscillations [1–23]  
<sup>17</sup> and indications of frequencies associated with solar rotation [14, 16]. On the other hand,  
<sup>18</sup> Bergeson et al. [24], Kossert and Nahle' [25], and Pomme' et al. [26] report negative  
<sup>19</sup> results (see also Sturrock et al. [27] for further discussion.) Additionally, a suggestion for  
<sup>20</sup> a possible solar influence on nuclear decays comes from observations of short-term changes  
<sup>21</sup> associated with solar storms [28, 29]. Although some questions have been raised concerning  
<sup>22</sup> the data supporting a solar influence [30–33], they have been addressed in the literature  
<sup>23</sup> [13, 21, 34]. As noted in Table II of Ref. [21], the indications of a possible solar influence on  
<sup>24</sup> radioactive decays come from experiments using a variety of detectors monitoring a number  
<sup>25</sup> of different radionuclides. One hypothesis which could account for these observations is that  
<sup>26</sup> they are due to the influence of solar neutrinos through some as yet unknown mechanism.  
<sup>27</sup> This motivates the study of decay rates in the presence of more readily available electron  
<sup>28</sup> antineutrinos [35, 36], including those produced by nuclear reactors.

<sup>29</sup>

<sup>30</sup> It is now well established that there exist three types of neutrinos denoted by  $\nu_e$ ,  $\nu_\mu$ ,  $\nu_\tau$   
<sup>31</sup> and their corresponding antiparticles  $\bar{\nu}_e$ ,  $\bar{\nu}_\mu$ ,  $\bar{\nu}_\tau$ . Additional types of neutrinos or neutrino-  
<sup>32</sup> like particles may exist such as sterile neutrinos [37] and neutrellos [38]. In what follows, we  
<sup>33</sup> describe a reactor experiment aimed at studying whether nuclear decay rates are influenced  
<sup>34</sup> by any light, neutral, and weakly interacting particle emitted by a reactor, including but  
<sup>35</sup> not limited to the presumably dominant  $\bar{\nu}_e$ . We note that the limits presented below on  
<sup>36</sup> perturbations induced by  $\bar{\nu}_e$  do not necessarily apply to the other neutrino flavors ( $\bar{\nu}_\mu$ ,  $\bar{\nu}_\tau$ , ...)  
<sup>37</sup> which may have significantly different properties (e.g. magnetic moments).

<sup>38</sup>

<sup>39</sup> Our experiment was carried out at the 85 MW (thermal) High Flux Isotope Reactor  
<sup>40</sup> (HFIR), located at Oak Ridge National Laboratory in Oak Ridge, Tennessee. This choice  
<sup>41</sup> was motivated in part by the opportunity to position our experiment sufficiently close to  
<sup>42</sup> the reactor core in order to achieve a  $\bar{\nu}_e$  flux comparable to or larger than the solar neutrino

<sup>43</sup> flux ( $\nu_{\odot}$ ). Additionally, the routine reactor-refueling outages introduce a convenient step  
<sup>44</sup> function in neutrino flux as the driving signal to generate the hypothetical perturbations.  
<sup>45</sup> Planning for the experiment began in October 2013 and our first run began in March 2014.  
<sup>46</sup> After initiating our reactor experiment at HFIR, we learned of reactor experiments by de  
<sup>47</sup> Meijer, Blau, and Smit [39], and by de Meijer and Steyn [40]. The more recent paper hints  
<sup>48</sup> at a positive effect.

<sup>49</sup>

<sup>50</sup> Phase I of this experiment, summarized in Appendix A, was an initial exploratory period  
<sup>51</sup> which focused on understanding various systematic effects such as backgrounds and the  
<sup>52</sup> sensitivity of our detectors to environmental conditions. Appendix A also describes many  
<sup>53</sup> aspects of the detectors and sources, along with the radioactive decay chains of the sources  
<sup>54</sup> used. The results presented here are derived from Phase II of this experiment, and due to its  
<sup>55</sup> extended duration of 217 days, (with five reactor ON periods and more accurate temperature  
<sup>56</sup> control), we achieved at least an order of magnitude better sensitivity in Phase II than in  
<sup>57</sup> Phase I.

## <sup>58</sup> **II. PHASE II EXPERIMENT**

<sup>59</sup> Phase II of our experiment from which our results below are derived took place between  
<sup>60</sup> August 2014 and March 2015 at HFIR. Analysis of  $^{152}\text{Eu}$  and  $^{241}\text{Am}$  data has been omitted  
<sup>61</sup> due to the relatively low energy of the chosen peaks, where the background is greater.  
<sup>62</sup> This experiment included eight of the 2 inch NaI(Tl) scintillation detectors with digIBASES  
<sup>63</sup> described in Appendix A. Each detector—except for the two background detectors—had a  
<sup>64</sup> radioactive source fixed securely to the front of the detector as in Appendix A. For Phase  
<sup>65</sup> II, to accomodate the then upcoming PROSPECT neutrino experiment, the detectors were  
<sup>66</sup> moved from site EF-4 to site EF-3 of the HFIR reactor, with the distance from the reactor  
<sup>67</sup> core increased from 5.8 m to 6.6 m, reducing the  $\bar{\nu}_e$  flux to approximately 46 times the solar  
<sup>68</sup>  $\nu$  flux at Earth. A new lead cave was constructed that consisted of two levels vertically with  
<sup>69</sup> four detectors on each level. To the sources in the original four bottom bays: Background  
<sup>70</sup> Counter 1,  $^{54}\text{Mn}$ ,  $^{60}\text{Co}$ , and  $^{152}\text{Eu}$ , we added in the top bays a second background detector, a  
<sup>71</sup> second  $^{54}\text{Mn}$  detector, a  $^{22}\text{Na}$  detetctor, and an  $^{241}\text{Am}$  detector (data from this last detector  
<sup>72</sup> were not analyzed because of low statistics and a very low energy spectrum). A styrofoam

<sup>73</sup> insulating box with 2 inch thick walls was built around the lead cave and maintained at  
<sup>74</sup> a stable temperature of  $20.00 \pm 0.03$  °C using a TECA thermo-electric unit with Watlow  
<sup>75</sup> PID controller. A schematic representation of the detectors' set up is shown in Table VI in  
<sup>76</sup> Appendix A.

<sup>77</sup>

<sup>78</sup> From the differential thermal expansion of the NaI-photomultiplier tube assembly rela-  
<sup>79</sup> tive to the enclosing aluminum can, we estimate displacement of the source relative to the  
<sup>80</sup> NaI to be  $1.95 \times 10^{-3}$  mm/K. At 4% per mm of source displacement, the resulting fractional  
<sup>81</sup> change in solid angle subtended by the NaI is  $-7.8 \times 10^{-5}$ /K. Thermal swelling of the NaI  
<sup>82</sup> increases the solid angle by  $9.5 \times 10^{-5}$ /K. The resulting net fractional change in counting  
<sup>83</sup> rate is  $1.7 \times 10^{-5}$ /K, or  $5.1 \times 10^{-7}$  per 0.3 K, which is negligible.

<sup>84</sup>

<sup>85</sup> Each of the eight detectors was connected to one of the four PCs at EF-3 via USB, and  
<sup>86</sup> each was programmed to run for one hour live-time intervals, where live-time is the real-  
<sup>87</sup> time as measured in the laboratory minus the dead-time as reported by the digiBASE. Each  
<sup>88</sup> detector thus runs for an interval greater than one hour, where the total real time is equal to  
<sup>89</sup> the fixed one hour of live-time plus the variable amount of dead-time added by the detector.  
<sup>90</sup> During this interval, the detector saves the output from the Multi-Channel Analyzer into a  
<sup>91</sup> time integrated 1024-bin histogram of energy. At the end of the time interval, information  
<sup>92</sup> from this histogram is saved into two different files: one report file and one spectrum file.  
<sup>93</sup> The spectrum file is simply a list of each of the 1024 bins and the counts recorded in each  
<sup>94</sup> of those bins, and the report file gives a shorter summary of the data. In both files, basic  
<sup>95</sup> information about the time interval is recorded, such as the date and time at which the  
<sup>96</sup> measurement interval began, as well as both the real-time and live-time for the interval.

<sup>97</sup>

<sup>98</sup> Along with the detector hardware, ORTEC also provides the MAESTRO software in order  
<sup>99</sup> to conveniently interact with their detectors. This software allows the user to set the high  
<sup>100</sup> voltage, gain, gain locking, and other properties of each detector. In addition, during a  
<sup>101</sup> measurement interval, the energy histogram (spectrum) is displayed on the screen option-  
<sup>102</sup> ally in either a linear or log scale. In order to make data acquisition and analysis easier,  
<sup>103</sup> MAESTRO allows the user to set custom Regions of Interest (ROIs) on the spectra for each  
<sup>104</sup> detector. At the end of each time interval when the report files are published, the total

105 counts for each ROI are summed over the specified energy range and reported. In addition to  
106 the integrated counts, MAESTRO fits a peak for the given ROI when a peak can be identified.  
107 MAESTRO reports a best fit for the centroid, full width at half maximum, and full width at  
108 fifth maximum, of the peak.

109

110 The ORTEC digIBASEs provide optional gain locking and zero locking. The gain locking  
111 and zero locking algorithms each prompt the user to identify an ROI containing a peak to  
112 which the software will then lock. As a counting interval begins, the gain locking software  
113 continuously attempts to find a peak within the locked ROI (the user also sets the width,  
114 in bins, of the peak fitting region). If the ROI contains a peak, the algorithm will adjust  
115 the fine gain settings of the detector in order to align the measured peak center with the  
116 peak center set by the user when the gain was originally locked. In high statistics running  
117 with gain locking, the fitted peak location is stable to a small fraction of one bin. Zero  
118 locking ensures that the zero of the detector does not drift—if an identifiable peak exists.  
119 The combination of gain locking and zero locking makes it possible to essentially eliminate  
120 drifts in the gain and zero of the detectors, making measurements much more accurate in  
121 the long run.

122

### 123 III. CORRECTING FOR DETECTOR-INDUCED RATE-DEPENDENT DISTOR- 124 TIONS IN THE MEASURED COUNTING RATE

125 As mentioned earlier, pileup and dead-time are known problems in counting-detectors,  
126 which worsen with higher counting rates. The digIBASE corrects for the dead-time, using  
127 a variant of the Gedcke-Hale algorithm. However, the MAESTRO/digIBASE system cannot  
128 correct for pileup effects. Pileup occurs when two photons which hit the detector close in  
129 time are not resolved, and the sum of their energies is registered as one event at a higher  
130 energy, and the other count is lost. The pileup effect is a rate-dependent convolution of the  
131 energy spectrum with itself. Whether the pileup adds to, or subtracts from, a given ROI is  
132 a complicated issue. In all of the ROIs used in our present data, the appearance of pileup is  
133 similar to the effect of less than  $2 \mu\text{s}$  excess dead-time erroneously added per count.

134

<sup>135</sup> To achieve sensitivities better than one part in  $10^4$ , we have chosen high overall counting  
<sup>136</sup> rates, up to 35 kHz, thereby entailing up to 13% dead-time and significant pileup. When  
<sup>137</sup> counting a given radioactive sample for a significant fraction of one half-life, we observe a  
<sup>138</sup> distortion in count rate relative to a pure exponential decay curve. The counting curve is  
<sup>139</sup> steeper than exponential early in the measurement, and less steep than exponential late in  
<sup>140</sup> the measurement.

<sup>141</sup> As noted in Appendix A, this distortion manifests itself in our data through half-life  
<sup>142</sup> measurements that are systematically low (larger decay constants), and which steadily  
<sup>143</sup> approach the published half-life values as the sample decays (as observed in our Phase I  
<sup>144</sup> experiment). These changes in decay constant are obviously purely instrumental and have  
<sup>145</sup> nothing to do with putative variations in the actual decay constant. We emphasize that  
<sup>146</sup> since the determination of precise decay constants was not the aim of this experiment, a  
<sup>147</sup> trade-off was made. Higher counting rates were chosen to give better statistical accuracy, to  
<sup>148</sup> better detect steps in the counting rate. The distortion can be well modeled by a correction  
<sup>149</sup> factor  $(1 + \alpha' \dot{N}_{tot})$  to be applied to the data to bring them into a pure exponential form.  
<sup>150</sup> The parameter  $\alpha'$  is typically 1.2 to 1.8  $\mu\text{s}$  where  $\dot{N}_{tot}$  is the overall counting rate into the  
<sup>151</sup> electronics. This pileup correction factor is algebraically equivalent to what would happen if  
<sup>152</sup> an excess dead-time of 1.2 to 1.8  $\mu\text{s}$  were erroneously added to the run time for each count,  
<sup>153</sup> in addition to approximately 4  $\mu\text{s}$  of actual dead-time correctly assigned by the detector  
<sup>154</sup> system. We emphasize that this form is a standard parameterization of the effects of pileup  
<sup>155</sup> [41], and that this does not mean that such excess dead-time is actually being added by the  
<sup>156</sup> digiBASE.

<sup>157</sup>

<sup>158</sup> The exact counting rate distortion factor used in the “Global Fit” of Section IV is  
<sup>159</sup>  $e^{\alpha C_{tot}(t)}$ , where  $C_{tot}(t) \equiv \dot{N}_{tot}(t) * 3600$  s is the total number of counts in one hour. To a  
<sup>160</sup> good approximation, the factor  $e^{\alpha C_{tot}}$  is identical to  $(1 + \alpha' \dot{N}_{tot})$  (the exponent is typically  
<sup>161</sup> 3% or less).  $\alpha'$  and  $\alpha$  differ by a factor of 3600 due to converting from counts per one-hour  
<sup>162</sup> interval to Hz. Either the  $\alpha$  or the  $\alpha'$  version can of course be used in the exponential form.  
<sup>163</sup> We choose the  $\alpha$  version for convenience.

<sup>164</sup>

<sup>165</sup> We emphasize that the rate-dependent distortion of the counting rate data is monotonic  
<sup>166</sup> with time, and secular, i.e. varies smoothly over the duration of the measurements. With

167 repeated ON/OFF cycles of the reactor, the hypothetical resulting multiple up and down steps  
 168 in counting rate allow the extraction of the parameter  $\epsilon$ , which is just the reactor ON vs. OFF  
 169 fractional change in counting rate, with minimal effect from the rate-dependent distortion.  
 170 The single parameter  $\alpha$ , which is sufficient to achieve excellent distortion adjustment, brings  
 171 the data into a smaller range of counting rates, allowing better visual inspection for residual  
 172 systematic effects, as well as making any steps more prominent.

#### 173 **IV. DETERMINATION OF THE PARAMETER $\epsilon$**

174 If the decay parameter,  $\lambda$ , changes in the presence of the reactor antineutrino flux, we  
 175 expect different slopes of the decay curve between reactor-ON and reactor-OFF periods. Note  
 176 that we measure the counting rate, which (if the solid angle subtended by the detector does  
 177 not change) is proportional to  $dN/dt$  where  $N(t)$  is the number of source nuclei as a function  
 178 of time. If  $\lambda$  is stepwise constant, i.e. alternates between values  $\lambda$  and  $\lambda'$  for reactor OFF  
 179 and ON, respectively, then the counting rate is proportional to:

$$\dot{N}(t) = \frac{dN}{dt} = \frac{d}{dt}(N_0 e^{-\lambda t}) = -\lambda N_0 e^{-\lambda t} \quad (\text{OFF}) \quad (1)$$

180 At the moment when the reactor turns ON if  $\lambda$  changes to  $\lambda'$ ,  $N(t)$  does not change  
 181 instantaneously. Hence the step in  $\lambda$  must cause a step in the counting rate, and we would  
 182 expect there to be a step in the counting rate each time there is a transition between ON  
 183 and OFF or vice versa. This is a much more sensitive way of searching for changes in  $\lambda$  than  
 184 through analysis of the slopes  $dN/dt$  themselves over time.

185

186 To capture the entire set of effects with optimal use of the data, we perform a four-  
 187 parameter Global Fit to the entire sequence of five ON and four OFF reactor periods. The  
 188 function used is a stepwise sequence of exponential decays with alternating decay parame-  
 189 ters  $\lambda$  and  $\lambda(1 + \epsilon)$ , where  $\epsilon \equiv (\lambda_{\text{ON}} - \lambda_{\text{OFF}})/\lambda_{\text{OFF}}$ . We have systematically excluded 8 hours  
 190 of data following each change in reactor status (ON-OFF or OFF-ON) to account for the  
 191 temporary time-dependences in  $\bar{\nu}_e$  flux as the reactor goes to full power, and for the time  
 192 after fission stops until the radioactive decay heat “afterglow” becomes negligible compared  
 193 to the 85 GW full power. The other two fitting parameters are  $C_0$ , the initial counts in one  
 194 hour; and the distortion parameter  $\alpha$  discussed in Section III. The exact formulas used are

<sup>195</sup> given in Appendix B.

<sup>196</sup>

## <sup>197</sup> V. ANALYSIS OF RESULTS

<sup>198</sup> Our results are presented in Figures 1-5. In Figure 1 we show the data from both <sup>54</sup>Mn  
<sup>199</sup> detectors, along with the <sup>22</sup>Na and <sup>60</sup>Co detectors (two peaks each) detrended by pure  
<sup>200</sup> exponentials using the fitted values of  $\lambda$ . These are simple 2-parameter fits with pileup and  
<sup>201</sup> perturbation parameters forced to zero:  $\alpha = 0$  and  $\epsilon = 0$ . The black curves are 20-point  
<sup>202</sup> moving averages. The residual “U-shaped” distortions are seen in the two <sup>54</sup>Mn plots. Given  
<sup>203</sup> the longer half-lives of <sup>22</sup>Na and <sup>60</sup>Co, we expect such distortions to be less apparent since  
<sup>204</sup> those counting rates have changed less during the experiment. ROI backgrounds based on  
<sup>205</sup> Detector 1 or 8 measurements are subtracted on an hourly basis. Modest uncertainties in  
<sup>206</sup> the background subtractions will be dealt with in our treatment of systematic uncertainties,  
<sup>207</sup> below. The full background treatment is given in Appendix C. Although we acquired data  
<sup>208</sup> from <sup>152</sup>Eu and <sup>241</sup>Am, their quality was relatively poor and hence they were not analyzed.

<sup>209</sup>

<sup>210</sup> Generally, the moving averages wander more than expected from purely statistical fluc-  
<sup>211</sup> tuations. In contrast, to make this visually clear and to ”calibrate the eye”, Figure 2 shows  
<sup>212</sup> Monte Carlo simulated pure exponential decays for the three radionuclides, with Gaussian  
<sup>213</sup> statistical fluctuations based on the hourly counts:  $3 \times 10^7$  (<sup>54</sup>Mn);  $1.2 \times 10^7$  (<sup>60</sup>Co);  $2.5 \times 10^7$   
<sup>214</sup> and  $4.0 \times 10^6$  for the <sup>22</sup>Na annihilation and gamma peaks, respectively. The scales of the  
<sup>215</sup> fluctuations in the simulations are much smaller than those in the measured data. Even  
<sup>216</sup> after de-trending the  $\alpha$  distortion, as seen in Figure 3, these irregularities in the actual data  
<sup>217</sup> are well above purely statistical, and hence must be systematic, and are of unknown origin.  
<sup>218</sup> The total fractional spread is small, ranging from 4 to 10 parts in  $10^4$ . The effects of these  
<sup>219</sup> systematics on  $\epsilon$  will be quantified below, in three different ways.

<sup>220</sup>

<sup>221</sup> The results of the Global Fits are shown in Tables I-III. The stated errors are purely  
<sup>222</sup> statistical, and the  $\chi^2/\text{dof}$  are all somewhat larger than, but close to, 1. The two main  
<sup>223</sup> <sup>60</sup>Co peaks are fitted separately, as are the <sup>22</sup>Na positron annihilation peak and the gamma  
<sup>224</sup> peak from the daughter nuclide. The values of  $\epsilon$  for the two <sup>22</sup>Na peaks are in reasonable

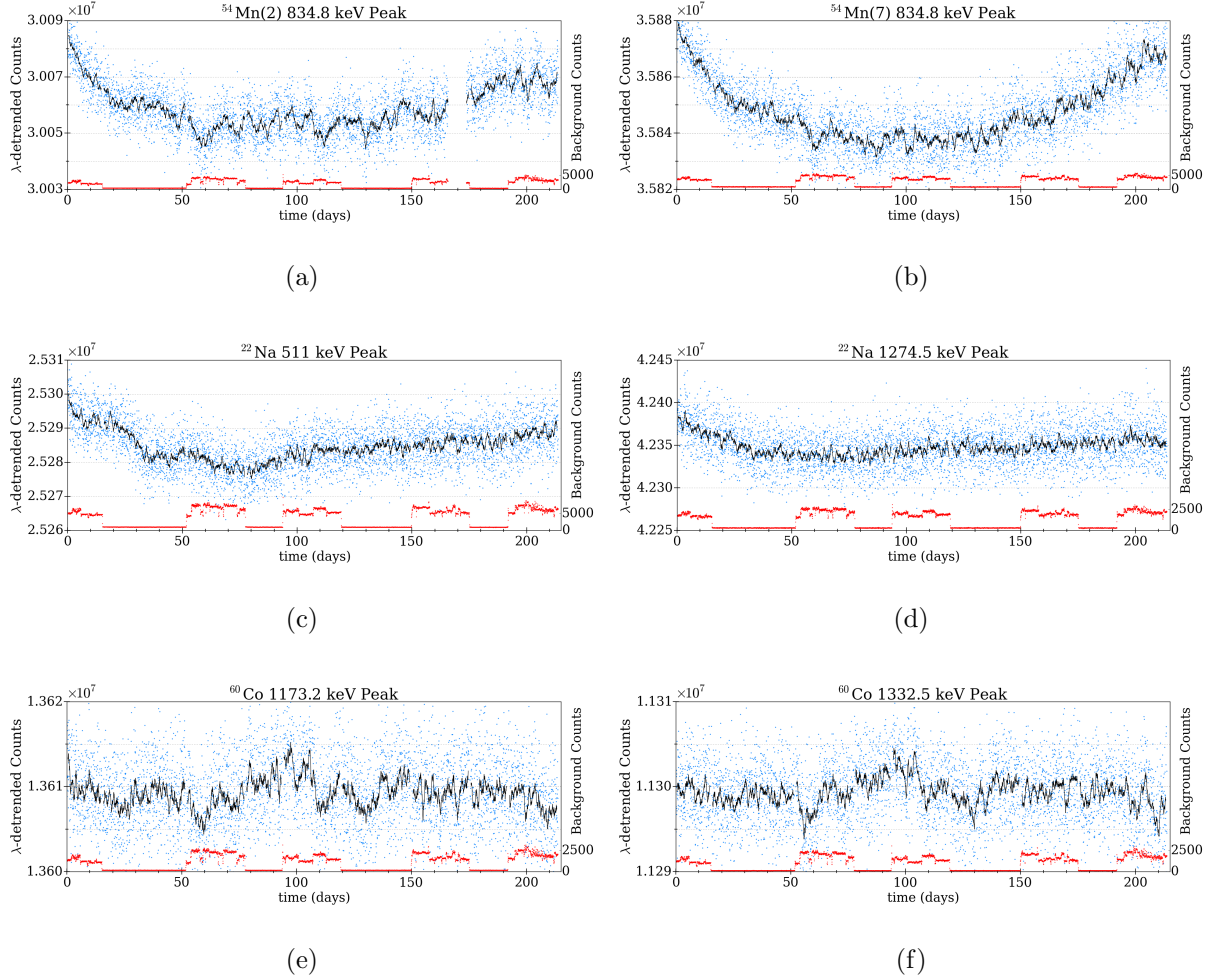


FIG. 1. Exponentially detrended hourly counts vs. time, [and the full vertical fractional intervals for]: (a)  $^{54}\text{Mn}$  Det.2 [ $2.0 \times 10^{-3}$ ] (b)  $^{54}\text{Mn}$  Det.7 [ $1.7 \times 10^{-3}$ ] (c)  $^{22}\text{Na}$  annihilation peak [ $2.0 \times 10^{-3}$ ] (d)  $^{22}\text{Na}$  gamma peak [ $4.7 \times 10^{-3}$ ] (e)  $^{60}\text{Co}$  low [ $1.4 \times 10^{-3}$ ] (f)  $^{60}\text{Co}$  high [ $1.8 \times 10^{-3}$ ]. The subtracted background amounts are plotted below the de-trended source plots, with identical vertical scales for comparison. The heavy black line is a 20-point moving average.

statistical agreement with each other, as are those for the two  $^{60}\text{Co}$  peaks. There is a high correlation between  $\lambda$  and  $\alpha$  for the two longer-lived radionuclides, which are relatively insensitive to  $\alpha$ . Hence, for more robust fitting, we fix the values of  $\alpha$  to be  $3.35 \times 10^{-10}$  ( $\alpha' = 1.2 \mu\text{s}$ ) as determined with good agreement by the fits for the two  $^{54}\text{Mn}$  detectors. With this choice, the half-lives of all four sources are fairly close to the published values, but differ from them (and in some cases, from each other) by several statistical standard deviations.

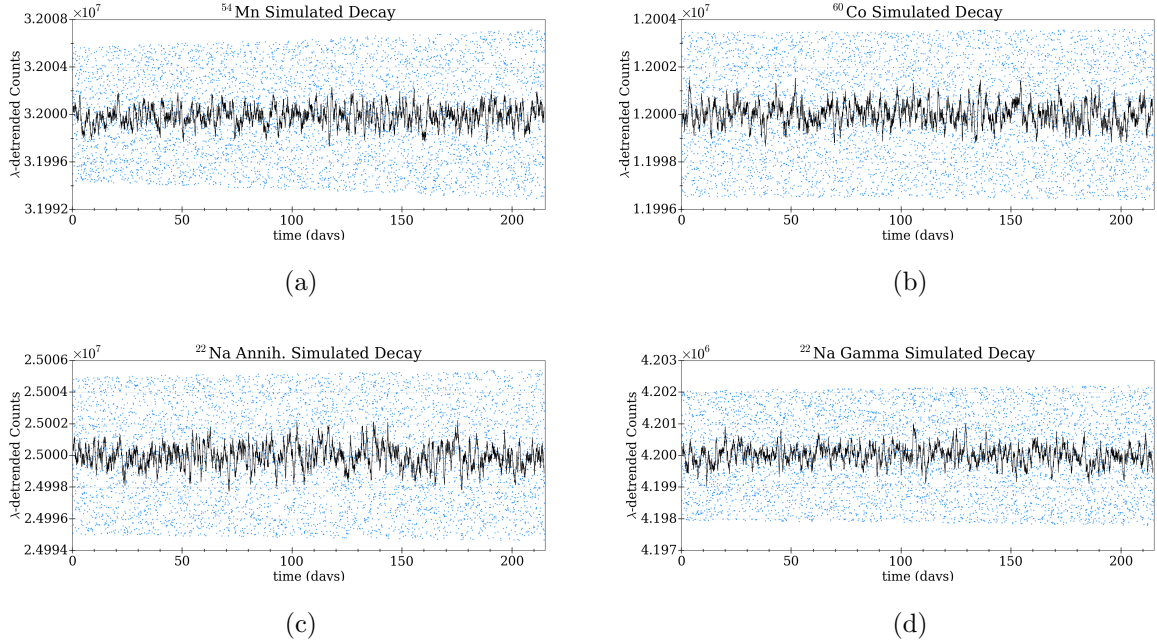


FIG. 2. Exponentially detrended Monte Carlo data series reflecting the Gaussian statistics of (a)  $^{54}\text{Mn}$  [ $3 \times 10^7$  hourly counts] (b)  $^{60}\text{Co}$  [ $1.2 \times 10^7$  hourly counts] (c)  $^{22}\text{Na}$  annih. [ $2.5 \times 10^7$  hourly counts] (d)  $^{22}\text{Na}$  gamma [ $4.2 \times 10^6$  hourly counts]. The total vertical fractional intervals are  $4.3 \times 10^{-4}$ ,  $6.7 \times 10^{-4}$ ,  $4.8 \times 10^{-4}$ , and  $1.4 \times 10^{-3}$ , respectively. The heavy black line is a 20-point moving average.

232

233     A. SYSTEMATIC ERRORS

234     Where possible, we use the data to make estimates of systematic errors from unknown  
 235 causes. We use three methods, described below. Additionally, we treat systematic errors  
 236 from three known possible causes. If we fix the decay constants to the published values,  
 237 as shown in Table II, thus changing from a 4-parameter to a 3-parameter fit, the values of  
 238  $\chi^2/\text{dof}$  increase by less than 1% for  $^{60}\text{Co}$  and  $^{22}\text{Na}$ , and by 3.6% and 6.7% for the two  $^{54}\text{Mn}$   
 239 detectors. The values of  $\alpha$  change modestly, but remain in the range of  $(3.3\text{-}5.5) \times 10^{-10}$ . The  
 240 values of  $\epsilon$  change, and we take the changes in  $\epsilon$  to be one of three estimates of the unknown  
 241 systematic errors: (1) “Fit Change” . The other two quantitative estimates of unknown  
 242 systematics are (2) the results of a “Shuffle Test” to be described below, and (3) the difference  
 243 between  $\epsilon$  values (“ $\Delta\epsilon$ ”) from the two  $^{54}\text{Mn}$  detectors,  $(4.98 \pm 0.83) \times 10^{-5}$ , and the two peaks

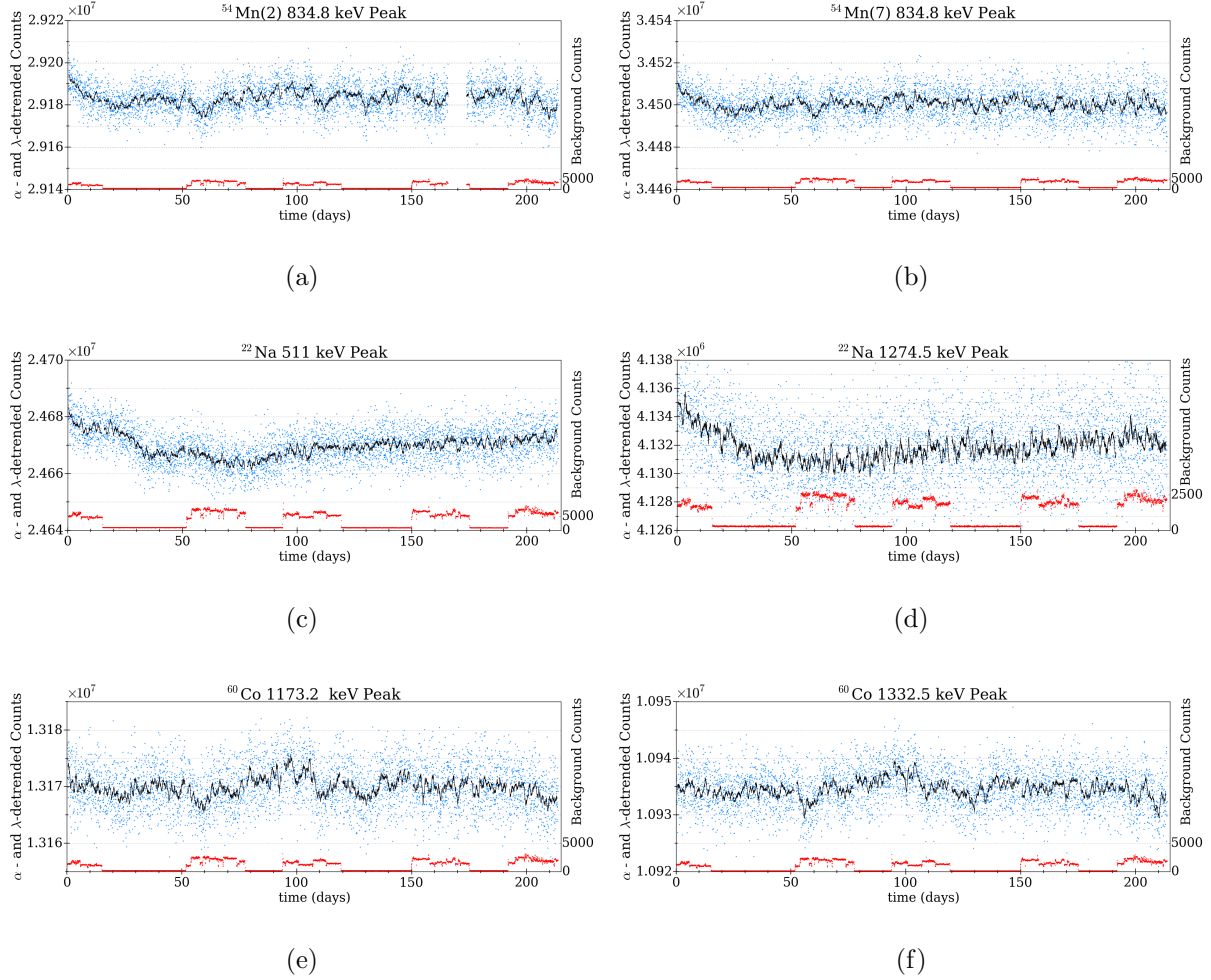


FIG. 3. Exponentially- and  $\alpha$ -detrended hourly counts vs. time, [and the full vertical fractional intervals for]: (a)  $^{54}\text{Mn}$  Det.2 [ $2.7 \times 10^{-3}$ ] (b)  $^{54}\text{Mn}$  Det.7 [ $2.3 \times 10^{-3}$ ] (c)  $^{22}\text{Na}$  annih. [ $2.4 \times 10^{-3}$ ] (d)  $^{22}\text{Na}$  gamma [ $2.9 \times 10^{-3}$ ] (e)  $^{60}\text{Co}$  low [ $2.3 \times 10^{-3}$ ] (f)  $^{60}\text{Co}$  high [ $2.7 \times 10^{-3}$ ]. The subtracted background counts are plotted below the de-trended source plots, with identical vertical scales for comparison. The heavy black line is a 20-point moving average.

each, in the  $^{60}\text{Co}$  and  $^{22}\text{Na}$  spectra,  $(1.31 \pm 1.25) \times 10^{-5}$  and  $(2.28 \pm 1.62) \times 10^{-5}$ , respectively. However,  $\Delta\epsilon$  for  $^{22}\text{Na}$  and  $^{60}\text{Co}$  are not statistically significant, and thus unlikely to represent systematic errors. Hence, to avoid “double counting” in these two cases, we propagate the  $\Delta\epsilon$  only for the comparison of the two  $^{54}\text{Mn}$  detectors. We note that for  $^{54}\text{Mn}$ ,  $\Delta\epsilon$  is 6 standard deviations from zero and a clear indication of some (unknown) systematic effect(s)

289 .

251 Three known systematic effects are: (1) due to the small uncertainties in the relative

TABLE I. Global Fit Results

radionuclide	Feature	$\lambda$ (days $^{-1}$ )	$C_0$	$\alpha$ (s)	$\epsilon$	$\chi^2/\text{dof}$	Half-life (d)	Published (d)
$^{54}\text{Mn}$	Det. 2	$2.23175 \times 10^{-3}$	$2.92 \times 10^7$	$3.224 \times 10^{-10}$	$-1.21 \times 10^{-5}$	1.295	310.58	312
	$\pm\sigma_{\text{stat}}^{\text{a}}$	$7.5 \times 10^{-7}$	$1.2 \times 10^4$	$4.4 \times 10^{-12}$	$6.2 \times 10^{-6}$		0.07	
	Det. 7	$2.23392 \times 10^{-3}$	$3.45 \times 10^7$	$3.472 \times 10^{-10}$	$4.05 \times 10^{-5}$	1.150	310.28	
		$7.0 \times 10^{-7}$	$1.3 \times 10^4$	$3.4 \times 10^{-12}$	$5.7 \times 10^{-6}$		0.07	
$^{22}\text{Na}$	511 keV	$7.29416 \times 10^{-4}$	$2.47 \times 10^7$	$3.35 \times 10^{-10}$	$2.96 \times 10^{-5}$	1.490	950.28	949.7
		$4.9 \times 10^{-8}$	$1.6 \times 10^2$		Fixed	$6.1 \times 10^{-6}$		0.04
	1275 keV	$7.39604 \times 10^{-4}$	$4.13 \times 10^6$	$3.35 \times 10^{-10}$	$6.3 \times 10^{-5}$	1.143	937.19	
		$1.2 \times 10^{-7}$	$6.5 \times 10^1$		Fixed	$1.5 \times 10^{-5}$		0.11
$^{60}\text{Co}$	1173 keV	$3.66119 \times 10^{-4}$	$1.32 \times 10^7$	$3.35 \times 10^{-10}$	$-1.26 \times 10^{-5}$	1.166	1893.23	1924.9
		$6.7 \times 10^{-8}$	$1.2 \times 10^2$		Fixed	$8.3 \times 10^{-6}$		0.24
	1333 keV	$3.67259 \times 10^{-4}$	$1.09 \times 10^7$	$3.35 \times 10^{-10}$	$1.74 \times 10^{-7}$	1.116	1887.35	
		$7.4 \times 10^{-8}$	$1.1 \times 10^2$		Fixed	$9.3 \times 10^{-6}$		0.26

<sup>a</sup> Statistical errors are given below fitted values in every row.

background levels in adjacent bays of the cave (see Appendix C). This, like the statistical errors, turns out to be negligible in quadrature with the three unknown-systematics estimates as we shall see below. (2) due to possible frequency shifts of the quartz crystal clock in the digiBASEs. A frequency shift would change the length of the live-time of a run, and hence the number of counts. Given the tight temperature control of the detectors, the manufacturer's specifications indicate better than 1 ppm frequency stability from thermal effects. Voltage dependence is less than 1 ppm for 5% variation of the voltage supplied to the oscillator circuit, which we take to be an upper limit on the stability of the USB voltage feeding the digiBASEs. Frequency shifts from aging of the quartz are less than 5 ppm in the first year, dominantly in the first two months. We take 5 ppm to be the upper limit on frequency shifts from all causes during the nine months duration of the data. Since this systematic error is both common to all detectors, and negligible compared to the dominant systematic errors, we omit it from the tables. (3) Gain locking, discussed in detail in Appendix D, by

TABLE II. Global Fit Results With  $\lambda$  Fixed to Published Value

radionuclide	Feature	$C_0$	$\lambda$ (days $^{-1}$ )	$\alpha$ (s)	$\epsilon$	$\chi^2/\text{dof}$	Published	Half-life
$^{54}\text{Mn}$	Det. 2	$2.90 \times 10^7$	$2.221 \times 10^{-3}$	$3.858 \times 10^{-10}$	$-2.23 \times 10^{-5}$	1.341	312 d	
	$\pm\sigma_{\text{stat}}^{\text{a}}$	$6.5 \times 10^2$	Fixed	$2.9 \times 10^{-13}$	$6.1 \times 10^{-6}$			
	Det. 7	$3.43 \times 10^7$	$2.221 \times 10^{-3}$	$4.102 \times 10^{-10}$	$2.75 \times 10^{-5}$	1.227		
		$6.9 \times 10^2$	Fixed	$2.2 \times 10^{-13}$	$5.6 \times 10^{-6}$			
$^{22}\text{Na}$	511 keV	$2.47 \times 10^7$	$3.601 \times 10^{-4}$	$3.265 \times 10^{-10}$	$3.05 \times 10^{-5}$	1.494	2.60 a	
		$1.6 \times 10^3$	Fixed	$9.6 \times 10^{-13}$	$6.1 \times 10^{-6}$			
	1275 keV	$4.07 \times 10^6$	$3.601 \times 10^{-4}$	$5.249 \times 10^{-10}$	$5.33 \times 10^{-5}$	1.127		
		$6.5 \times 10^2$	Fixed	$2.3 \times 10^{-12}$	$1.5 \times 10^{-5}$			
$^{60}\text{Co}$	1173 keV	$1.30 \times 10^7$	$7.299 \times 10^{-4}$	$5.051 \times 10^{-10}$	$-1.24 \times 10^{-5}$	1.161	5.27 a	
		$2.3 \times 10^3$	Fixed	$1.9 \times 10^{-12}$	$8.3 \times 10^{-6}$			
	1333 keV	$1.07 \times 10^7$	$7.299 \times 10^{-4}$	$5.371 \times 10^{-10}$	$-6.82 \times 10^{-7}$	1.112		
		$2.1 \times 10^3$	Fixed	$2.1 \times 10^{-12}$	$9.4 \times 10^{-6}$			

<sup>a</sup> Statistical errors are given below fitted values in every row.

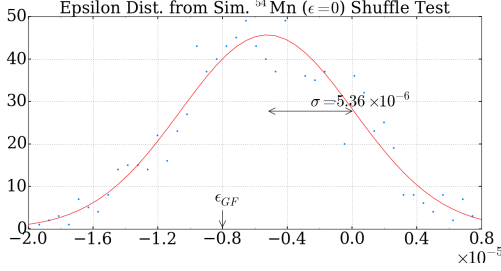
the MAESTRO/digibase system is almost perfect, but there are slight gradual drifts seen in the fitted positions of the main peaks in the spectra, whereas the ROI boundaries are fixed. This can in principle cause shifts in the counting rate if the bin contents at the two edges of the ROI are not equal. However, the drift in counting rate is small, steady, and monotonic over the entire data-taking period. Hence it will have a completely negligible effect on the values of the fitted step-size parameter,  $\epsilon$ , so we omit this from the subsequent analysis.

271

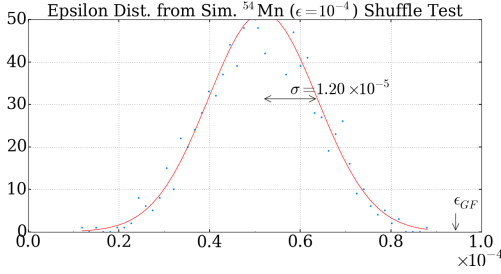
## 272 B. SHUFFLE TEST

273 In order to further quantify the uncertainty of our results, we subject our data to a modified version of a standard Shuffle Test [42, 43]. We randomly shift the ON/OFF transition 274 times from the actual values. Each transition time is shifted randomly with uniform weight 275

in a restricted interval. The first interval is from the start of the entire data set to the midpoint between the first and second transition times; the second interval extends from this midpoint to the next one, etc. For each random choice of transition times, a Global Fit is performed. This is repeated 1000 times and the distribution of  $\epsilon$  values is plotted. Since in general the shifted transition times treat a fraction of the ON state as OFF, and OFF as ON, any genuine reactor effect on the decay rate would tend to be diluted, driving the value of  $\epsilon$  closer to zero, or even to the opposite sign if there is a preponderance of wrong assignments of both reactor states. In general, one would *not* expect the magnitude of  $\epsilon$  from a genuine reactor effect to be increased by the shuffle;  $\sqrt{N}$  Gaussian statistics alone cannot drive values of  $\epsilon$  larger than the best fit value in a shuffle test. To demonstrate this, two simulated decay sets were generated with a value of  $\lambda$  equal to that of  $^{54}\text{Mn}$ , one with no steps and one with  $\epsilon = 1 \times 10^{-5}$ . The statistics were determined by Gaussianly distributing the counts about the exponential, with  $\sqrt{N}$  statistics and  $N_0 = 3 \times 10^7$  counts per hour. The resulting data streams were then processed by the Global Fitting procedure described above. The dilution of  $\epsilon$  (i.e. suppression) by incorrect transition times is clearly seen in Fig.4; for the non-zero- $\epsilon$  case,  $\epsilon$  is never more than the input value (the no-step sequence has a “shuffle sigma” much smaller than all the others, reflecting the absence of systematic errors). Figure 5 shows the frequency distributions of  $\epsilon$  for the three radionuclides. All six distributions are reasonably fitted by Gaussians. For the two  $^{60}\text{Co}$  peaks, the values of  $\epsilon$  are widely distributed on either side of the (small) Globally Fitted values, with standard deviations ( $\sigma$ ) of  $3.6 \times 10^{-5}$  and  $4.2 \times 10^{-5}$ . We consider these deviations as estimates of the effects of the visible systematic fluctuations in the de-trended data. Note that these standard deviations are considerably larger than the Globally Fitted statistical uncertainties. The  $^{22}\text{Na}$  shuffle distributions, in more than half of the cases, *increase* the values of  $\epsilon$ , clearly impossible for a genuine reactor effect. The Gaussian  $\sigma$ 's are  $6.9 \times 10^{-5}$  and  $7.9 \times 10^{-5}$ , again considerably larger than the Globally Fitted statistical errors. For the  $^{54}\text{Mn}$  in Detector 2, the value of  $\sigma$  is  $3.0 \times 10^{-5}$  and many values of  $\epsilon$  are greater than the Globally Fitted value, comparable to the other radionuclides. For Detector 7 the  $\sigma$  from the Shuffle Test is  $1.6 \times 10^{-5}$ , and in a significant number of cases  $\epsilon$  is greater than the Globally Fitted value—again incompatible with a genuine reactor effect. It will be seen in the following section on error propagation, that the shuffle estimates of uncertainty are dominant for all six measurements of  $\epsilon$ .



(a)



(b)

FIG. 4. Distributions of  $\epsilon$  from Global Fits to 1000 Monte Carlo random shuffles of the reactor transition times for two simulated data sets: (a)  $\epsilon = 0$  (b)  $\epsilon = 10^{-4}$ . Both use typical  $^{54}\text{Mn}$  counting rates [ $3 \times 10^7$  hourly counts]. The Globally Fitted values of  $\epsilon$  are shown with arrows on the x-axis, which is the  $\epsilon$ -axis. The y-axis is in arbitrary units.

308     C. ERROR PROPAGATION

309     As discussed above, some of the systematic error estimates come from the differences in  
 310 two values of  $\epsilon$ : the “Fit Change” from the two alternative Global Fits, as shown in Table  
 311 III. Also as seen in Table III there is a discrepancy in the measured values of  $^{54}\text{Mn}$   $\epsilon$  between  
 312 Detectors 2 and 7. This unknown systematic error, presumed random, is estimated using the  
 313 “scatter” of two values, we apply the formula [44] for the corrected and unbiased estimator  
 314 of  $\sigma$ , from two samples:

$$\sigma = \frac{s}{C_4(N)}. \quad (2)$$

315 With

$$s = \sqrt{\frac{\sum(x_i - \bar{x})^2}{N-1}} \quad \text{and} \quad C_4(N) = \sqrt{\frac{2}{N-1}} \frac{\Gamma(\frac{N}{2})}{\Gamma(\frac{N-1}{2})}, \quad (3)$$

316 it follows from Eq. (3) that

$$\sigma = \frac{|x_1 - x_2|}{1.128} \quad (4)$$

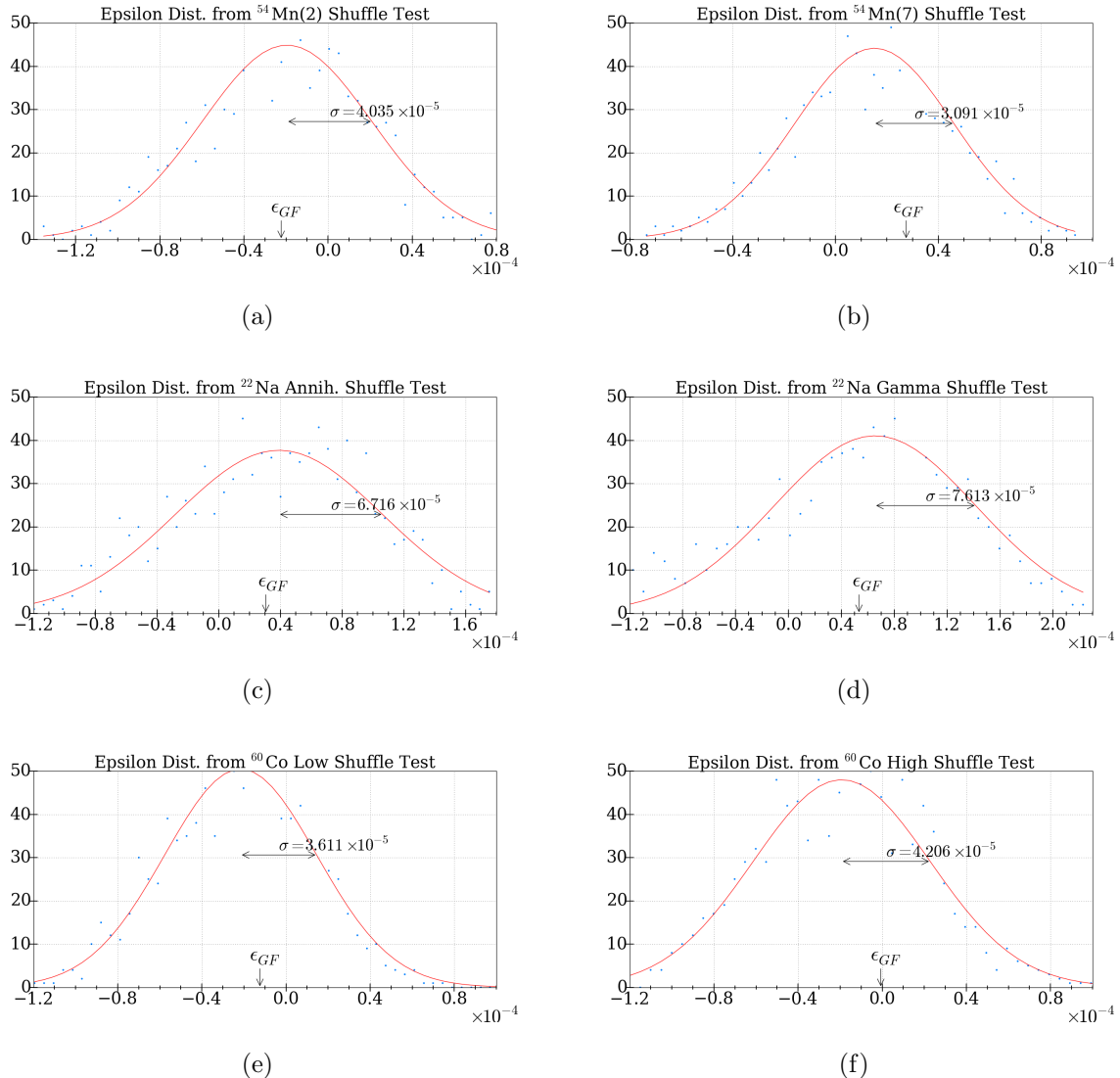


FIG. 5. Distributions of  $\epsilon$  from Global Fits to 1000 Monte Carlo random shuffles of the reactor transition times for: (a)  $^{54}\text{Mn}$  Det.2 (b)  $^{54}\text{Mn}$  Det.7 (c)  $^{22}\text{Na}$  annih. (d)  $^{22}\text{Na}$  gamma (e)  $^{60}\text{Co}$  low (f)  $^{60}\text{Co}$  high.

for  $N = 2$ . This gives  $\sigma = |\epsilon_{\text{Det}7} - \epsilon_{\text{Det}2}|/1.128 = 4.41 \times 10^{-5}$  from the two  $^{54}\text{Mn}$  detectors.

318

319 The values of  $\epsilon$  from the six peaks are given in Table III, together with their statistical  
 320 errors and three of the four types of systematic error discussed above. The known systematic  
 321 clock frequency stability uncertainty of  $\pm 5$  ppm which is common to all detectors, is negli-  
 322 gible and is not included in the table. Also shown are the statistically weighted averages of  
 323 the two  $\epsilon$  values for each radionuclide. The background systematic errors are propagated in

TABLE III. Epsilons with All Errors

radionuclide	Feature	statistical uncertainties		systematic uncertainties		
		$\epsilon$	$\pm$ stat.	Bkgd.	Fit Change	Shuffle
$^{54}\text{Mn}$	Det. 2	$-2.23 \times 10^{-5}$	$6.1 \times 10^{-6}$	$2.6 \times 10^{-6}$	$9.1 \times 10^{-6}$	$4.04 \times 10^{-5}$
	Det. 7	$2.75 \times 10^{-5}$	$5.6 \times 10^{-6}$	$2.3 \times 10^{-6}$	$1.2 \times 10^{-5}$	$3.09 \times 10^{-5}$
	Average	$4.80 \times 10^{-6}$	$4.1 \times 10^{-6}$	$3.5 \times 10^{-6}$	$1.5 \times 10^{-5}$	$5.08 \times 10^{-5}$
$^{22}\text{Na}$	511 keV	$3.05 \times 10^{-5}$	$6.1 \times 10^{-6}$	$4.2 \times 10^{-6}$	$7.9 \times 10^{-7}$	$6.72 \times 10^{-5}$
	1275 keV	$5.33 \times 10^{-5}$	$1.5 \times 10^{-5}$	$9.0 \times 10^{-6}$	$8.6 \times 10^{-6}$	$7.61 \times 10^{-5}$
	Average	$3.38 \times 10^{-5}$	$5.6 \times 10^{-6}$	$1.0 \times 10^{-5}$	$4.7 \times 10^{-6}$	$7.43 \times 10^{-5}$
$^{60}\text{Co}$	1173 keV	$-1.24 \times 10^{-5}$	$8.3 \times 10^{-6}$	$3.0 \times 10^{-6}$	$1.9 \times 10^{-7}$	$3.61 \times 10^{-5}$
	1333 keV	$6.82 \times 10^{-7}$	$9.4 \times 10^{-6}$	$3.3 \times 10^{-6}$	$7.6 \times 10^{-7}$	$4.21 \times 10^{-5}$
	Average	$-7.24 \times 10^{-6}$	$6.2 \times 10^{-6}$	$4.4 \times 10^{-6}$	$4.7 \times 10^{-7}$	$3.90 \times 10^{-5}$

In the statistical uncertainties section, a weighted average is given below the  $\epsilon$  and  $\pm$  stat. columns for each radionuclide. In the corresponding rows of the systematic uncertainties section, the errors are summed in quadrature for each radionuclide.

324 quadrature for each radionuclide. The differences in  $\epsilon$  for  $^{22}\text{Na}$  and  $^{60}\text{Co}$  are not statistically  
 325 significant, which is not surprising since the same detector is measuring both peaks for the  
 326 radionuclide. Note that the Shuffle Test systematic errors are quite similar within a given  
 327 detector. The Fit Change estimates for  $^{22}\text{Na}$  and  $^{60}\text{Co}$  are small and will contribute little to  
 328 the overall uncertainty. The 1275 keV Na data also have small statistical weight relative to  
 329 the more abundant positron annihilation peak. Since some of the unknown systematic errors  
 330 are probably common to a given detector, we use the mean of the two Shuffle uncertainties in  
 331 the summary lines for  $^{22}\text{Na}$  and  $^{60}\text{Co}$  in Table III, and similarly for the Fit Change column.  
 332 Further justification for this choice can be seen in parts (c),(d) of Fig. 3: the long-term  
 333 features of the  $^{22}\text{Na}$  data for the two peaks are similar, showing some degree of correlation.  
 334 In parts (e),(f) of this figure, for the two  $^{60}\text{Co}$  peaks, the shorter term fluctuation patterns  
 335 appear rather similar, again showing some degree of correlation. The case is not so clear for  
 336  $^{54}\text{Mn}$ , since two different detectors are involved; but the values of the uncertainties in each  
 337 of the two columns are nearly equal. Moreover, the  $^{54}\text{Mn}$  parts of the figure, (a),(b) show

<sup>338</sup> some degree of correlation, with an initial drop followed by a dip at around day 70 in both  
<sup>339</sup> detectors (the dip at around day 70 is also present for the Co plots (e),(f)). In any case, we  
<sup>340</sup> conservatively propagate the Fit Change and Shuffle errors for  $^{54}\text{Mn}$  in quadrature.

## <sup>341</sup> VI. CONCLUSIONS

<sup>342</sup> Table IV summarizes the three values of  $\epsilon$  from the three radionuclides. The statistical  
<sup>343</sup> errors, and the small systematic errors in relative bay-to-bay background levels, are both  
<sup>344</sup> almost insignificant when added in quadrature to each of the estimates of unknown sys-  
<sup>345</sup> tematic errors for each radionuclide. Note that because there is no significant statistical  
<sup>346</sup> discrepancy between detectors, the  $\Delta\epsilon$  estimates for  $^{22}\text{Na}$  and  $^{60}\text{Co}$  are not used, to avoid  
<sup>347</sup> “double counting”. We quote the final results for  $\epsilon$  as two-sided 95% C.L. “outer limits”  
<sup>348</sup> (mean value  $\pm 2 \times$  overall  $\sigma$ ).

<sup>349</sup>

<sup>350</sup> In summary, while this experiment is quite sensitive statistically, given the estimated  
<sup>351</sup> systematic errors the 95% CL outer limits are plus or minus one or two parts in  $10^4$  on  
<sup>352</sup> perturbations in  $\beta^\pm$  decay (or electron capture) processes, in the presence of an antineutrino  
<sup>353</sup> flux of  $3 \times 10^{12} \text{ cm}^{-2}\text{s}^{-1}$ . Our  $10^{-4}$  exclusion level is roughly comparable to that of de Meijer  
<sup>354</sup> and Steyn [40], who find for  $^{22}\text{Na}$  a relative change between reactor-ON and reactor-OFF  
<sup>355</sup> of  $(-0.51 \pm 0.11) \times 10^{-4}$  (which translates to outer limits  $[-0.73, -0.29] \times 10^{-4}$ ) , but do not  
<sup>356</sup> exclude possible systematic errors. In a more recent paper, de Meijer et al. [45] find a much  
<sup>357</sup> larger non-zero value:  $(-3.04 \pm 0.26(\text{stat}) \pm 0.03(\text{syst})) \times 10^{-4}$  which is in contradiction to  
<sup>358</sup> our present outer limits for  $^{22}\text{Na}$ ;  $[-1.12 \times 10^{-4}, 1.79 \times 10^{-4}]$ ; (and to their original result.)  
<sup>359</sup> A non-null measurement is outside the Standard Model of particles and forces, and calls  
<sup>360</sup> for further measurements of  $^{22}\text{Na}$  decay. If we define an effective “cross section”  $\sigma_e$  to  
<sup>361</sup> characterize the change  $\Delta\lambda$  in  $\lambda$  induced by a change  $\Delta\phi$  in antineutrino flux,  $\sigma_e = \frac{\Delta\lambda}{\Delta\phi}$ , then  
<sup>362</sup> we find for our experiment  $\sigma_e \lesssim 9 \times 10^{-25} \text{ cm}^2$ , which compares to  $\sigma_e = (2.9 \pm 0.6) \times 10^{-25}$   
<sup>363</sup>  $\text{cm}^2$  [or  $(1.7 \pm 0.15) \times 10^{-24} \text{ cm}^2$ ] cited in the first [or second] papers by de Meijer et al.  
<sup>364</sup> If we assume that the interaction strength of  $\bar{\nu}_e$  with radioactive radionuclides is the same  
<sup>365</sup> as that of  $\nu_e$ , then our upper limit excludes  $\nu_e$  as the dominant source of the  $\mathcal{O}(10^{-3})$   
<sup>366</sup> effects reported in some of the original papers [1–23, 28, 29]. However, as noted in the  
<sup>367</sup> Introduction, our results do not impose any constraints on the coupling strengths of other

TABLE IV. Final Epsilons

radionuclide	$\epsilon$	Total error	95% LL	95% UL
$^{54}\text{Mn}$	$4.80 \times 10^{-6}$	$6.91 \times 10^{-5}$	$-1.33 \times 10^{-4}$	$1.43 \times 10^{-4}$
$^{22}\text{Na}$	$3.38 \times 10^{-5}$	$7.27 \times 10^{-5}$	$-1.12 \times 10^{-4}$	$1.79 \times 10^{-4}$
$^{60}\text{Co}$	$-7.24 \times 10^{-6}$	$3.98 \times 10^{-5}$	$-8.69 \times 10^{-5}$	$7.24 \times 10^{-5}$

368 neutrino flavors, which are present in both the solar neutrino flux, and as components in the  
 369 cosmic neutrino background, but are not significantly present 6 m from the HFIR reactor  
 370 core. The present experimental methods are applicable to a wide variety of radioactive  
 371 radionuclides. Further measurements, with even tighter control of environmental variables  
 372 and smaller backgrounds, are being planned. Given the small statistical uncertainties of the  
 373 present method, an improvement in sensitivity can be anticipated as we continue to reduce  
 374 the dominant systematic uncertainties.

375      **Appendix A: Phase I Experiment**

376      We summarize in this Appendix the features of the Phase I experiment which also apply  
377 to the Phase II experiment from which our final results were derived. Table V presents  
378 details of the decay data of sources used in this experiment. Data acquisition in Phase  
379 I commenced on 15 March 2014 at 04:24 with the reactor ON and continued through the  
380 reactor shutdown (23 March 2014 at 05:23) until 30 March 2014. This provided for an  
381 on/off comparison of the decay rates of the radioactive radionuclides that were studied. In  
382 Phase I the decay rates of three radioactive radionuclides were studied:  $^{54}\text{Mn}$  which decays  
383 by electron capture (EC),  $^{60}\text{Co}$  which decays by beta-emission ( $\beta^-$ ), and  $^{152}\text{Eu}$  which has  
384 significant branching to both EC (72.10%) and  $\beta^-$  decay (27.90%). The nuclides were  
385 chosen, in part, from indications in earlier experiments [1–23] that each had exhibited a  
386 time variation in its decay constant, possibly due to solar neutrinos. In Phase II, described  
387 in the body of the text, we added detectors with  $^{22}\text{Na}$  and a second  $^{54}\text{Mn}$  source.

388

389      Further motivation for the choice  $^{54}\text{Mn}$  comes from an apparent correlation between  
390 changes in the  $^{54}\text{Mn}$  decay rate and the solar storm of 13 December 2006 [28] and subse-  
391 quent storms [29]. This radionuclide is also of interest since its dominant decay mode is  
392 electron capture, and hence allows a comparison to the radionuclide  $^{60}\text{Co}$ , which is a pure  
393  $\beta^-$  decay. Cobalt-60, in turn, was selected on the basis of the observation by Parkhomov of  
394 an annual variation in its decay [46]. Finally, the choice of  $^{152}\text{Eu}$  was dictated by the fact  
395 that this radionuclide decays via both EC and  $\beta^-$  modes. Moreover, the data presented by  
396 Seigert *et al.* [3] indicate periodicity in the intensity (count rate) of the 1408 keV  $\gamma$  emitted  
397 in the EC process. This particular observation is especially interesting since the periodic  
398 signal, obtained using a Ge(Li) detector, was observed to be 180 days out of phase with the  
399 data taken by the same group on  $^{226}\text{Ra}$  and its daughters using a  $4\pi$   $\gamma$ -ionization chamber  
400 [3]. Additionally, radionuclides were preferred which decayed to the excited state of the  
401 daughter nucleus. This would ensure that the  $\beta-$ decay of the parent could eventually be  
402 recorded by the photons emitted in the nuclear de-excitation of the daughter to its ground  
403 state. Since such a decay produces a sharp peak at a well-defined energy, this allowed us  
404 to focus on a relatively narrow region-of-interest (ROI) in the  $\gamma$ -spectrum whose location in  
405 a Multi-Channel Analyzer (MCA) could be identified and controlled. Among radionuclides

TABLE V. Decay Data of Sources Used in This Experiment. The notation (g.s.) describes a transition to the ground state of the daughter nucleus.

$^{54}_{25}\text{Mn} + e^- (\text{EC}) \rightarrow ^{54}\text{Cr}^* + \nu_e$ (100%)	$T_{1/2} = 312$ d
$\hookrightarrow ^{54}_{24}\text{Cr(g.s.)} + \gamma(834.8 \text{ keV})$	
$^{22}_{11}\text{Na} \rightarrow ^{22}_{10}\text{Ne} + e^+ + \nu_e$ (90%)	$T_{1/2} = 2.60 \text{ a} = 949.7 \text{ d}$
$\hookrightarrow e^+e^- \rightarrow \gamma\gamma(511 \text{ keV})$	
$^{22}_{11}\text{Na} + e^- (\text{EC}) \rightarrow ^{22}_{10}\text{Ne}^* + \nu_e$ (10%)	
$\hookrightarrow ^{22}_{10}\text{Ne(g.s.)} + \gamma(1274.5 \text{ keV})$	
$^{60}_{27}\text{Co} \rightarrow ^{60}_{28}\text{Ni}^* + e^- + \bar{\nu}_e$ ( $\sim 100\%$ )	$T_{1/2} = 5.27 \text{ a} = 1924.9 \text{ d}$
$\hookrightarrow ^{60}_{28}\text{Ni(g.s.)} + \gamma(1173.3 \text{ keV}) + \gamma(1332.5 \text{ keV})$	
$^{152}_{63}\text{Eu} + e^- (\text{EC}) \rightarrow ^{152}_{62}\text{Sm}^* + \nu_e$ (73%)	$T_{1/2} = 13.54 \text{ a} = 4945 \text{ d}$
$\hookrightarrow ^{152}_{62}\text{Sm(g.s.)} + \gamma(122 \text{ keV})$	
$^{152}_{63}\text{Eu} \rightarrow ^{152}_{64}\text{Gd}^* + e^- + \bar{\nu}_e$ (27%)	
$\hookrightarrow ^{152}_{64}\text{Gd(g.s.)} + \gamma(779 \text{ keV})$	

whose decays suggest interesting effects,  $^3\text{H}$ ,  $^{32}\text{Si}$ , and  $^{36}\text{Cl}$  are decays with no photons, and thus not suited to be detected by our NaI crystal scintillators. These considerations led to our selection of  $^{54}\text{Mn}$ ,  $^{60}\text{Co}$ , and  $^{152}\text{Eu}$  in Phase I, joined by  $^{22}\text{Na}$  in Phase II.

409

410 Particular attention was devoted to  $^{54}\text{Mn}$  ( $T_{1/2} = 312\text{d}$ ) with which we had the most  
411 extensive experience from our previous experiments at Purdue.  $^{54}\text{Mn}$  decays via electron  
412 capture and is detected via the chain exhibited in Table V.

413

414 We note in passing that our choices led to a set of radionuclides with a broad range of  
415 half-lives:  $^{54}\text{Mn}$  (312 d),  $^{22}\text{Na}$  (2.60 a),  $^{60}\text{Co}$  (5.27 a),  $^{152}\text{Eu}$  (13.54 a). All published half-  
416 lives are taken from Ref. [47]. The sources have activities of several  $\mu\text{Ci}$  ( $1 \text{ Ci} = 3.7 \times 10^{10}$   
417 decays per second) and give counting rates of order 20 to 35 kHz, which entail detector  
418 dead-times in the range 10% to 13%. The sources were encapsulated in standard 1-inch  
419 diameter plastic discs.

420

421 In Phase I of this experiment the apparatus consisted of four detectors, including one  
422 with no source mounted as a control and to measure background counting rates. The  
423 detectors were St. Gobain/BICRON 2 inch NaI(Tl) crystal plus photomultiplier, sealed  
424 assemblies, in 2.25 inch diameter cylindrical aluminum cans. Each detector was coupled  
425 to a digiBASE (ORTEC), an electronically gain-locked PMT base, including high voltage  
426 supply, preamplifier, and multichannel analyzer. Dead-time in the system was corrected by  
427 implementation of a variant of the Gedcke-Hale live-time clock, which extended the running  
428 time of a measurement cycle until the requested live-time was achieved. Data acquisition  
429 across all detectors was performed with software MAESTRO (ORTEC) running on one central  
430 personal computer, connected to the PMT bases via USB.

431

432 The source discs were each mounted on a triangular metal plate affixed to three thin  
433 standoffs matching the periphery of the front end of the detector can. These standoffs were  
434 then affixed to the edge of the front face of the can. The objective was to avoid motion of  
435 the source by possible barometric flexing of the front disc of the sealed can. (This had been  
436 seen to happen if the source is mounted directly to the center of the front disc, with small,  
437 concomitant but significant fluctuations in counting rate.) The objective of the experiment  
438 was to be sensitive to fluctuations in counting rates fractionally smaller than  $10^{-3}$ . This  
439 requires very stable geometry of the source position relative to the detector: a simple geo-  
440 metrical calculation shows that a point-like source located 6 mm from a 50 mm diameter, 50  
441 mm long crystal (typical of our assemblies), and displaced 1 mm towards or away from the  
442 crystal, sees a change in the subtended solid angle of  $\pm 4.8\%$  at the front face of the crystal,  
443 and  $\pm 3.14\%$  at the back face of the crystal. This represents an average of  $\pm 4\%$  per 1 mm  
444 motion, or as a useful mnemonic, 1 part per thousand per 0.001 inches (25  $\mu\text{m}$ ) of motion.

445

446     Background suppression was achieved by surrounding each detector by at least 4 inches  
447 (10 cm) of lead. Moreover, the detectors were separated from one another by 4 inches of  
448 lead to mitigate cross-talk in a structure, referred to as the cave, with four bays (see Fig.  
449 6 for details). Altogether, approximately 1.8 metric tons of lead were required, using 150  
450 standard  $2 \times 4 \times 8$  inch<sup>3</sup> lead bricks.

451

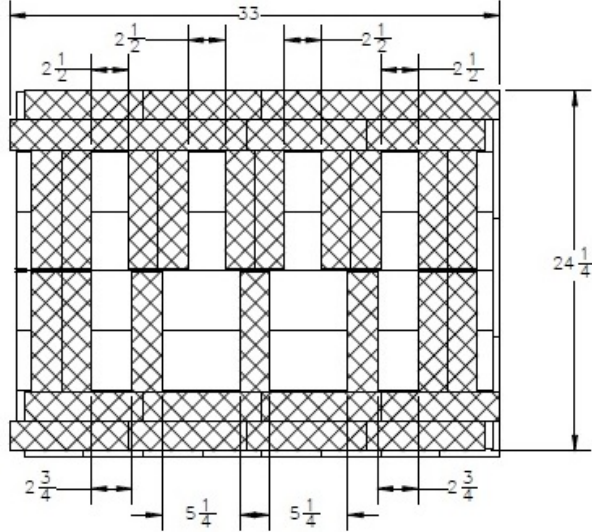
452     With the reactor ON, backgrounds outside the cave were typically a few thousand counts  
453 per second (cps). The lead shielding was effective in reducing the background by nearly  
454 3 orders of magnitude, and we conservatively mounted the background detector in the  
455 highest-count bay (bay #1). The gain of the background counter was set lower than any  
456 of the other detectors, so that it was sensitive to any gamma ( $\gamma$ ) energy that would arise  
457 from any of our radionuclides. The counting rate refers to the entire spectral range of the  
458 background counter, whereas only portions of the background will fall in the regions of  
459 interest (ROIs) used for counting.

460

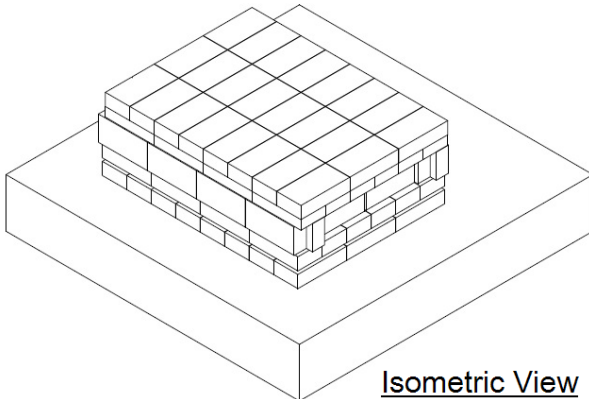
461     The total counting rates from backgrounds inside the cave were small, of order  $10^{-3}$   
462 of the counting rates from the sources. Hence in Phase I, background estimates were  
463 not subtracted from the source counts, although they were in Phase II, from which our  
464 final results were obtained. Moreover, fluctuations in the interior background rates were  
465 less than 20% of the average background level, and were believed to be associated with the  
466 intermittent operation of a neutron beam line passing one floor below in the reactor building.

467

468     The lead cave and the detector array were situated 5.83 m from the HFIR reactor core  
469 at site EF-4, directly along one of the reactor-core center lines, 4 m higher than the core  
470 and 4.27 m away laterally. The core is a cylinder 20 cm in diameter and 40 cm in height,  
471 which we treat approximately as point-like for flux calculations. Calculations by our group  
472 and others [48] of the total  $\bar{\nu}_e$  flux from highly enriched uranium reactors give a  $\bar{\nu}_e$  flux at  
473 5.8 m from HFIR, at 85 MW thermal output, of  $3.8 \times 10^{12} \text{ cm}^{-2} \text{ s}^{-1}$ , which is 58 times larger  
474 than the solar  $\nu$  flux at Earth,  $6.5 \times 10^{10} \text{ cm}^{-2} \text{ s}^{-1}$ , and 830 times larger than the 7% annual  
475 variation in the solar  $\nu$  flux due to the Earth's orbital eccentricity. Since the power of the  
476 HFIR reactor is known to be constant, it is presumed that the  $\bar{\nu}_e$  flux is as well.



(a)



(b)

FIG. 6. (a) Schematic drawing of the layout of each detector bay within the lead cave. Hashing denotes lead bricks and open regions denote spaces for the NaI detectors. Dimensions are given in inches. (b) Diagram of the lead cave in Phase I. The large block under the cave represents the floor.

477

478 As noted above, primary data acquisition started on 15 March 2014 at 04:24 EDST  
 479 with the reactor already ON, and consisted of a continuous stream of 30 minute (live-time)  
 480 cycles. Each cycle produced a  $\gamma$  energy spectrum, and a table of counts from each of a set of  
 481 selected ROIs (i.e. groups of bins in the energy spectrum). The reactor ran at approximately  
 482 85 MW thermal power (see Fig. 7) until it was shut down at 06:00 on 23 March 2014.

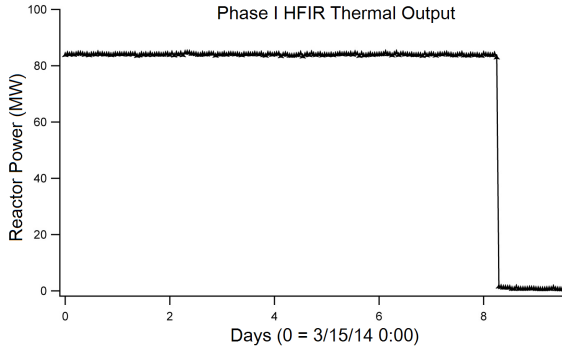


FIG. 7. HFIR thermal power (MW) output for a 10 day test run. The HFIR reactor was shut down for routine maintenance on 23 March 2014, at 06:00, which corresponds to day 8.25 on the above graph.

483 Thermal power dropped to 0.2 MW in the succeeding three hours and then effectively to  
 484 zero, presumably reflecting the initial part of the afterglow arising from short-lived fission  
 485 products. Data acquisition then continued in the OFF period until 30 March 2014.

486

487 Residual  $\bar{\nu}_e$  flux from the spent core is expected to be below 1%. Although multiple spent  
 488 cores are stored at the other end of the reactor pool in which the reactor operates, they  
 489 are at distances from our detectors several times the distance of the operating reactor. The  
 490 most recently extracted core emits copious Cherenkov radiation as seen from the observation  
 491 gallery, however the next most recent core shines only dimly. The ages of the spent cores  
 492 increase in increments of roughly two months. Suppression of  $\bar{\nu}_e$  flux due to decay time and  
 493 distance were estimated to outweigh the increase in  $\bar{\nu}_e$  flux due to the number of spent cores  
 494 stored in the pool, as seen at our detectors.

495

496 Temperature control of the detector-source assembly is very important. Differential  
 497 thermal expansion of the NaI(Tl) crystal mounted onto a glass PMT envelope, versus the  
 498 surrounding aluminum can, will partly but not necessarily completely cancel shifts of the  
 499 front end of the can relative to the crystal. Sodium iodide has a larger expansion coefficient,  
 500 and glass has a lower coefficient, compared to aluminum. Also, expansion of the NaI(Tl)  
 501 crystal will increase the solid angle subtended. The temperature at the experimental lo-  
 502 cation was climate controlled within approximately 2 °C and, as monitored at one of the  
 503 detectors inside the lead cave, remained within a 0.2 °C range for most of the period while

504 the reactor was on. This climate control in the hall was unexpectedly discontinued (due to  
505 HVAC failure) when the reactor was shut down, following which the temperature measured  
506 by the sensor located at bay #4 in the lead cave rose by 6 °C from day 9 to day 15, in  
507 two stages, and then started to drop. This motivated incorporation of an independent  
508 temperature control for the Phase II experiment.

509

510 We conclude this section with a brief summary of the Phase I results as they relate to  
511 the subsequent Phase II experiments. A more complete description of the Phase I data can  
512 be found in [49]. In addition to the importance of independent temperature control noted  
513 above, the Phase I data highlighted the importance of dead-time and pileup effects in our de-  
514 tectors. Specifically, the 312 d half-life of  $^{54}\text{Mn}$  was sufficiently short that the  $\sim 10\%$  change  
515 in counting rate over the course of a  $\sim 1$  month run produced changes in dead-time/pileup  
516 corrections that had to be modeled more carefully at the sensitivity levels we were aiming  
517 to achieve. The specific indication for the more detailed modeling of dead-time and pileup  
518 to be described below, was the observation that the Phase I data did not reproduce the  
519 accepted 312 d  $^{54}\text{Mn}$  half-life when the reactor was in the OFF mode, as we had expected.  
520 The half-lives and decay modes of the nuclides studied in both Phase I and Phase II are  
521 presented in Table V. We do not include  $^{241}\text{Am}$  due to the very low energy of the relevant  
522 gamma peaks, where backgrounds are large.

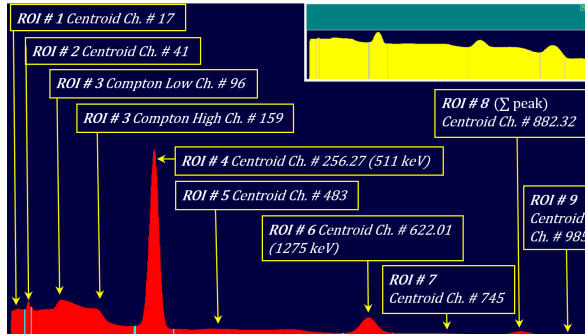
523

524 The primary signal for an ON/OFF antineutrino effect at HFIR in Phase I would have been  
525 a systematic difference between the  $^{54}\text{Mn}$  half-life (and others) associated with the reactor  
526 ON compared to reactor OFF. However, necessity for the aforementioned pileup/dead-time  
527 corrections led to implementation of a superior criterion for an ON/OFF signal: the presence  
528 of a step-function change in the  $^{54}\text{Mn}$  (and other) decay rates associated with an ON/OFF  
529 or OFF/ON transition in the HFIR power. The magnitude of this change, reflected by the  
530 parameter  $\epsilon$  introduced below, is relatively insensitive to the gradual changes that arise from  
531 the long term secular changes in pileup/dead-time corrections due to the decay of the  $^{54}\text{Mn}$   
532 sample.

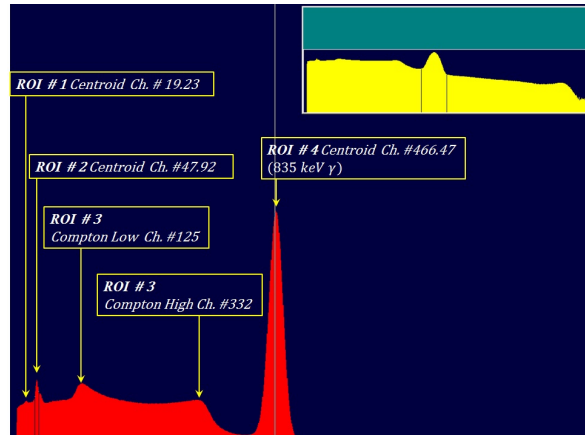
533

TABLE VI. Detector Layout

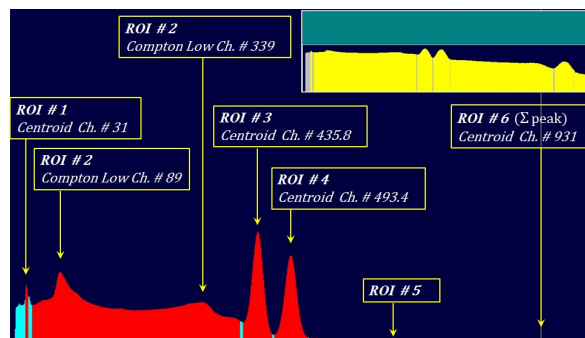
Detector 5 $^{241}\text{Am}$	Detector 6 $^{22}\text{Na}$	Detector 7 $^{54}\text{Mn}$	Detector 8 Background	Top Layer
Detector 1 Background	Detector 2 $^{54}\text{Mn}$	Detector 3 $^{60}\text{Co}$	Detector 4 $^{152}\text{Eu}$	Bottom Layer



(a)



(b)



(c)

FIG. 8. Energy spectra with chosen ROIs for: (a)  $^{22}\text{Na}$  (b)  $^{54}\text{Mn}$  (c)  $^{60}\text{Co}$ . The x axis is energy channel number in bins 1 through 1024; the y axis is counts per channel on a linear scale.

534      **Appendix B: The Global Fitting Formalism**

535      The Global Fitting formulas described in Section V uses just four parameters:  $C_0$  (the  
 536 initial counts in one hour); the decay constant,  $\lambda_0 \equiv \lambda_{\text{OFF}}$ ;  $\epsilon \equiv (\lambda_{\text{ON}} - \lambda_{\text{OFF}})/\lambda_{\text{OFF}}$ ; and  
 537 the parameter  $\alpha$  used in the rate-dependent distortion factor described in Section III. We  
 538 measure the counting rates in the form of the dimensionless number of counts in each one  
 539 hour of live time.

540

541      To illustrate the functional form of the Global Fit, assume that an experiment began in  
 542 an OFF period and lasted for a time  $T_1$ , followed by an ON period which lasted for a time  
 543  $T'_1$ . Then at the end of the first ON and OFF periods we have for OFF<sub>1</sub>

544

$$N(T_1) = N_0 e^{-\lambda_0 T_1} \quad (\text{B1})$$

545 and for ON<sub>1</sub>,

$$N(t) = N(T_1) e^{-\lambda_0(1+\epsilon)(t-T_1)} = N_0 e^{-\lambda_0[t+\epsilon(t-T_1)]} \quad (\text{B2})$$

$$N(T_1 + T'_1) = N_0 e^{-\lambda_0[(T_1 + T'_1) + \epsilon T'_1]}. \quad (\text{B3})$$

546      The first term of the exponential in Eq.(B3) gives the surviving number of atoms after a  
 547 cumulative time  $(T_1 + T'_1)$  starting from  $N_0$ , assuming no influence from reactor antineutrinos.  
 548 For  $\epsilon > 0$  assumed, the  $\epsilon$ -dependent contribution then gives an additional loss during  
 549 the time  $T'_1$  due to the excess in the decay constant,  $\lambda_0\epsilon$ . The results in Eqs.(B1-B3) can  
 550 be generalized in an obvious way: the number of surviving atoms  $N(t)$  after a cumulative  
 551 elapsed time  $t$  is given by

552

$$N(t) = N_0 e^{-\lambda_0(t+\epsilon \sum_i T'_i)} \quad (\text{B4})$$

553      In Eq.(B4),  $\sum_i T'_i$  extends over only ON periods  $T'_i$ , during which it is assumed that any  
 554 additional reactor-ON contributions enter with the same factor  $\epsilon$ . For the HFIR reactor at  
 555 Oak Ridge this assumption is justified given that during each ON period the reactor runs at

556 the same 85 MW rate using the same fuel composition.

557

558 What is actually measured is the counting rate, or its proxy, the hourly count total  $C(t)$ .

559 Incorporating the counting rate dependent distortion factor described in Section III,  $e^{\alpha C(t)}$

560 gives

561

562 for OFF periods:

563

$$C(t) = C_0 e^{-\lambda_0(t+\epsilon \sum_i T'_i) + \alpha C(t)} \quad (\text{B5})$$

564 and for ON periods:

565

$$C(t) = C_0(1 + \epsilon) e^{-\lambda_0(t+\epsilon \sum_i T'_i) + \alpha C(t)}. \quad (\text{B6})$$

566 Once again,  $\sum T'_i$  is the sum of all ON time intervals up to the data point at time  $t$ .

567 **Appendix C: Background Subtractions**

568 As can be seen in Figs. 1 and 3, the backgrounds from a variety of sources are small  
569 and steady in the reactor-OFF periods. However, backgrounds during reactor-ON periods  
570 are larger and highly irregular due to several intermittently-operated neutron beam lines  
571 one floor below the detectors. The general effect of such backgrounds, if not dealt with,  
572 could mimic an increased decay rate during reactor-ON periods, and could thus generate  
573 false steps and a spurious positive value of  $\epsilon$ . Although background effects at HFIR and  
574 other high power research reactors have been studied previously by Ashenfelter et al. [50],  
575 we felt that it was important to make detailed measurements at the specific sites of our  
576 detectors, given that backgrounds can vary from place to place at a reactor such as HFIR.  
577 Two counters, with no installed sources, were located in bays #1 and #8, on the lower and  
578 upper levels, respectively, of the cave—as in Table VI. We use the background information  
579 on an hour-by-hour basis.

580 At the start of Phase II, which was during a reactor-ON period, each of the two back-  
581 ground counters was placed in each of the eight bays of the lead “cave”, to measure the

TABLE VII. Ratio of Initial Background Counts Relative to Detector 1. See text for further discussion.

Det5 Am: 0.917	Det6 Na: 0.871 <sup>b</sup>	Det7 Mn: 0.951	Det1 Bkg: 1.0000 <sup>a</sup>	$\pm 0.020$
Det1 Bkg: 1.0000 <sup>a</sup>	Det2 Mn: 0.895	Det3 Co: 0.936	Det4 Eu: 1.075	$\pm 0.024$

<sup>a</sup> Top row ratios are relative to Bay 8 and bottom row ratios are relative to Bay 1

<sup>b</sup> For the Na annih. peak, background subtraction is done with Det. 8 data, and the initial ratio relative to Det. 8 is 0.911.

TABLE VIII. Gains relative to Detector 1 (2.646 keV/bin). See text for further discussion.

Det5 Am: 9.093	Det6 Na: 1.326	Det7 Mn: 2.412	Det8 Bkg: 4.260
Det1 Bkg: 1.000	Det2 Mn: 1.478	Det3 Co: 0.979	Det4 Eu: 1.042

relative background levels. The results as measured by Detector 8 are shown in Table VII, where the background-level scale factors of the top row are relative to bay #8 and the bottom row scale factors are relative to bay #1. These original calibration runs had five minute live times, and in Detector 1 typically had approximately 4800 counts in top-row bays and 3500 counts in bottom-row bays. The resulting statistical uncertainties in Table VII are 2.0% for the top row and 2.4% for the bottom row. These uncertainties lead to one type of systematic error on  $\epsilon$ , shown in Table III, which is quantified by varying the amount of background subtracted for the Global Fit analysis. The relative gains of all eight detectors are well measured and any gain-induced uncertainties will contribute negligibly to the sizes of the background subtractions.

592

593 The lower four counters are better shielded than the upper-level counters, by two lead layers instead of one. Also, central bays are more shielded than side bays. In general we expect the central bays to have somewhat smaller background counting rates than the side bays, and the top row of bays generally to have significantly larger background levels than the bottom row. The gain of Detector 1 is set near or lower than any of the other gains, to cover all background energies that could lie at one of the source detectors' main gamma peaks. The gain of Detector 8 is larger than any of the other gains (4.26 times the gain of Detector 1), and hence Detector 8 does not cover the energy range of almost all of the peaks

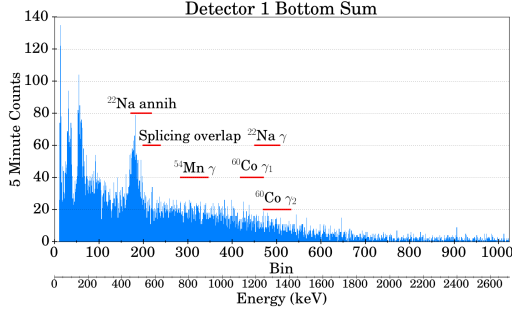
of interest in counters with radioactive sources (with the exception of the  $^{22}\text{Na}$  positron annihilation peak). Detector 8 can be used directly for the  $^{22}\text{Na}$  annihilation peak. For the  $^{22}\text{Na}$  gamma peak and the Detector 7  $^{54}\text{Mn}$  peak, we can approximately recover the missing Detector 8 information by using the Detector 1 information, scaled up by the ratio of counts in an overlap region defined by bins 860 to 1023 in Detector 8. This maps approximately onto bins 202 through 240 of the Detector 1 spectrum. Since the gains of the detectors are all different, we must of course map a given ROI onto the corresponding energy range in the relevant background counter. Additionally one must also take careful account of fractional bin contents. We can justify the the use of Detector 1 data to replace missing Detector 8 data as follows: The Detector 1 spectra measured in bays 1 through 4 (Bottom) are summed, and similarly for bays 5 through 8 (Top), and are shown in Fig. 9. The spectral shapes are very similar, both in the scaling region and also in all energy regions of interest, as is seen in the Top/Bottom ratio plot of this figure.

614

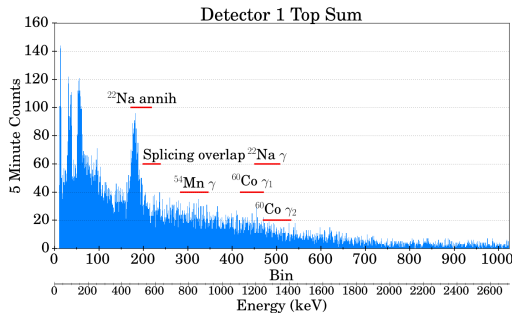
From the main running periods, we have much higher background statistics by summing spectra from several days of running, and this allows us to study the reactor-OFF backgrounds. Such summed background spectra for both detectors for ON and OFF are shown in Fig. 10. During ON periods, the spectrum is rather smoothly decreasing after the last peak (which is somewhat below bin 200 in Detector 1). The chosen overlap scaling region is shown as a horizontal red bar, as are the various energy regions of interest. The OFF period background levels are some five times lower than for the ON period, and the spectrum falls off more quickly and has very little of the structure just below bin 200 in Detector 1. Hence the scaling/splicing procedure should work equally well, or better during OFF periods.

624

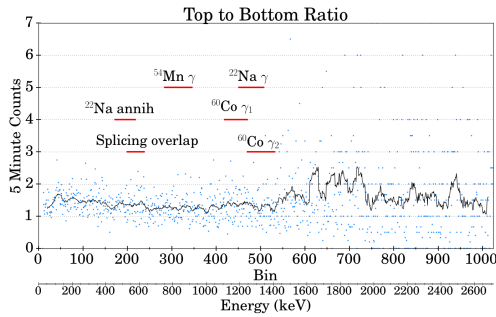
The Detector 1 gain locking was set for a peak in bin 54, which is present when the reactor is ON. This peak is absent when the reactor is OFF. In the absence of the chosen peak, the gain locking algorithm mistakenly recognizes a peak in bin 13, and it very slowly and steadily (due to the very low statistics) increases the gain. This can be seen in Fig. 11, where the gain increases by some 12 % over the first 32-day OFF period. When the reactor turns ON, the gain is restored fairly quickly (due to the five times higher counting rate). This gain drift is easily corrected for in the subsequent analysis, by rescaling the energy spectrum after the fact using the observed gains. The Detector 8 gain locking worked perfectly, and



(a)



(b)



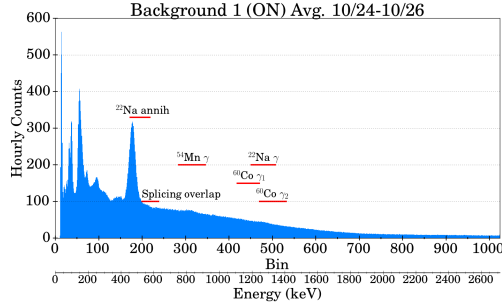
(c)

FIG. 9. Various sums of reactor-ON spectra from 5 minute initial Phase II background runs with Detector 1 in all eight bays of the the cave: (a) Sum of top bays (b) Sum of bottom bays (c) Ratio of top sum to bottom sum. Energy regions of interest and the Det1-Det8 scaling overlap region are shown as horizontal bars. The heavy black line is a 20-point. moving average.

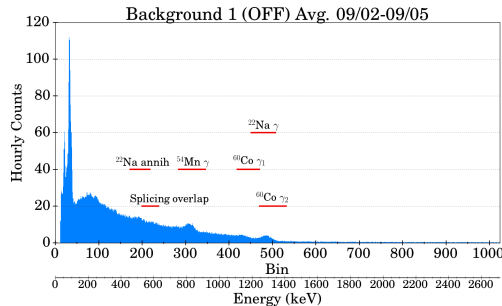
633 no correction was needed.

634

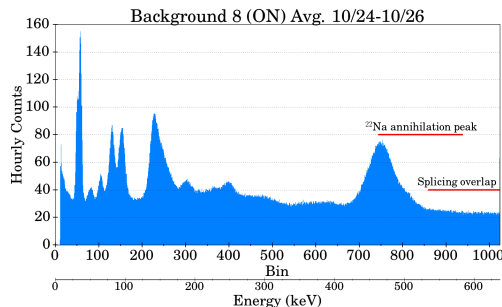
635 The counters run asynchronously, with different dead-times (and negligible dead-time for  
 636 the background counters.) Thus more than a single one-hour background count period is  
 637 matched to a given source count period. Background information is taken from these over-



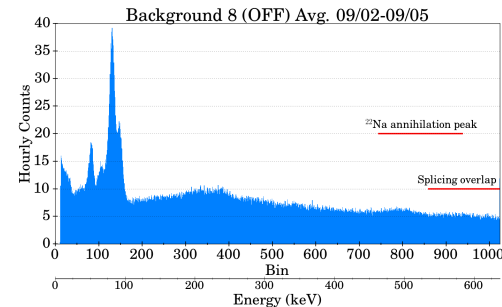
(a)



(b)



(c)



(d)

FIG. 10. 3-day sums of background spectra for reactor-ON and -OFF with Detector 1 in bay 1 and Detector 8 in bay 8: (a) Det. 1 ON (b) Det. 1 OFF (c) Det. 8 ON (d) Det. 8 OFF. Energy regions of interest and the Det1-Det8 scaling overlap region are shown as horizontal bars.

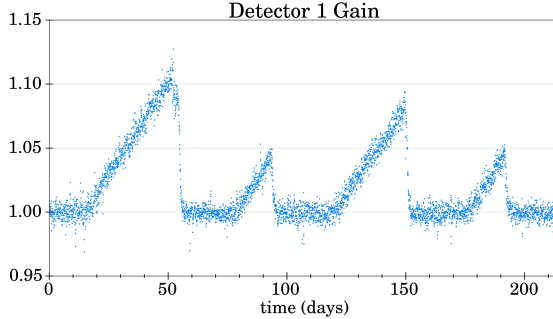


FIG. 11. Hourly gain values of background Detector 1 vs. time, which are used to correctly map ROIs onto the background spectrum. Detector 8, not shown, had no gain variations.

638 lapping periods in such a way that only 60 minutes of live background counts are considered.

639

640 **Appendix D: Gain Locking Systematics**

641 The gain locking of the digiBASE is excellent, but not perfect. It will be seen below that  
 642 the effects of the observed tiny drifts in peak positions cause very small, gradual, fractional  
 643 changes in the counting rates over the entire data taking period. This should have negligible  
 644 effects on the fitted size of any steps in the counting rates. Typical changes in the fitted  
 645 peak positions are a few hundredths of a spectral bin width (Fig. 12), with the exception of  
 646 the higher energy  $^{60}\text{Co}$  and  $^{22}\text{Na}$  peaks, which have overall (and nonlinear) drifts of 0.12 and  
 647 0.14 of a bin width, respectively, which are still small. The gain is being locked for only one  
 648 ROI (peak) per detector; if there are slight nonlinear changes in gain across the spectrum,  
 649 the higher peaks can drift slightly. The report files used to make the plots list the peak  
 650 position to the nearest hundredth of a bin width, as can be seen from the quantization of  
 651 the levels in the figure. The scatter of a few hundredths of a bin width from hour to hour,  
 652 presumably due to the statistics in the peaks, is sufficient to support linear least square fits  
 653 to the data for four of the peaks, from which we read off beginning and ending peak posi-  
 654 tions. For the worst-case upper  $^{60}\text{Co}$  and  $^{22}\text{Na}$  peaks, we easily extract the total drift by eye.

655

656 The results are presented in Table IX. The fractional effects on the counting rates over  
 657 the entire data taking period are in all cases less than  $1.1 \times 10^{-4}$ . This has a completely  
 658 negligible effect on the determination of  $\epsilon$ , and we omit this systematic error from the

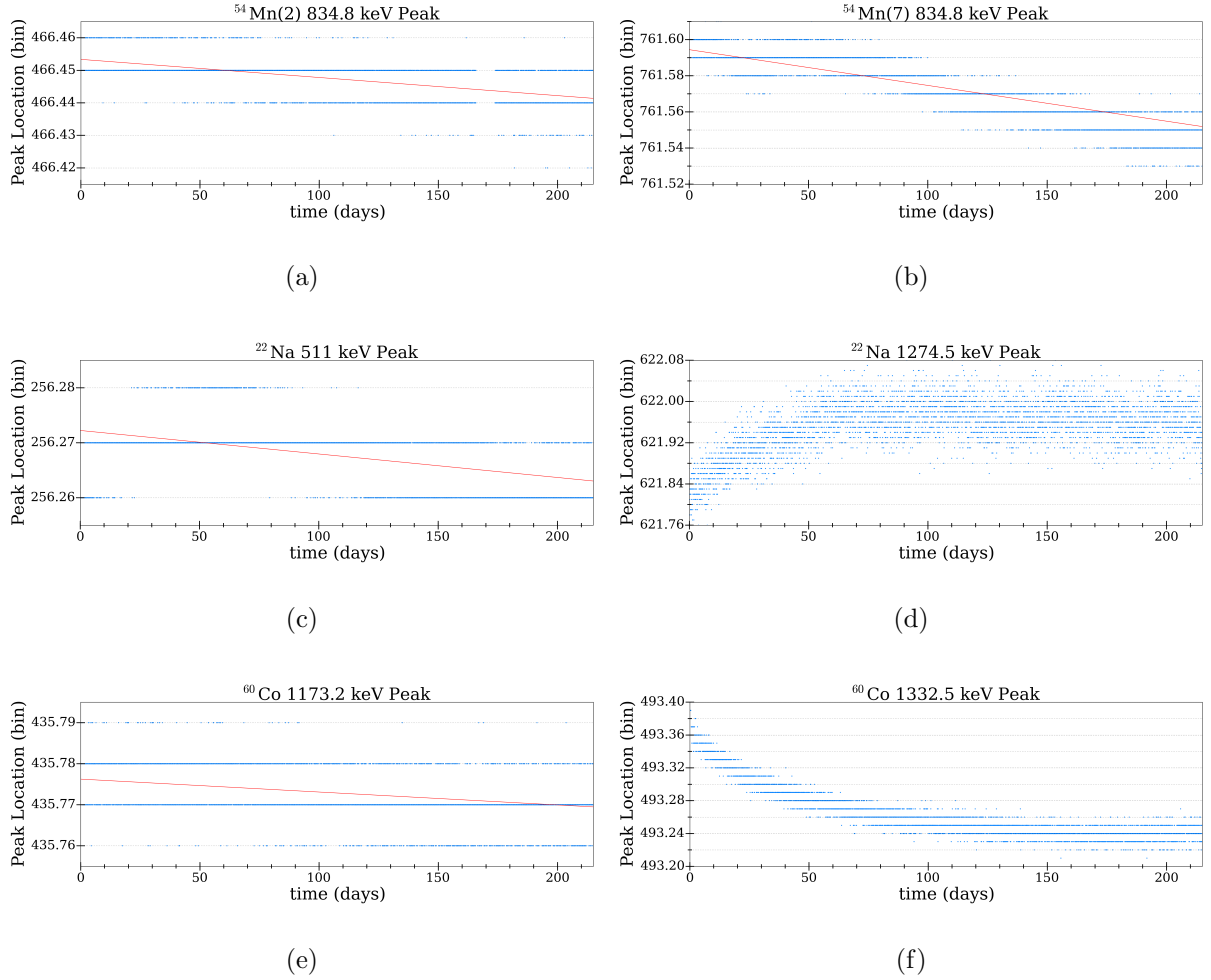


FIG. 12. Peak locations as recorded by MAESTRO for: (a)  $^{54}\text{Mn}$  Det.2 (b)  $^{54}\text{Mn}$  Det.7 (c)  $^{22}\text{Na}$  annih. (d)  $^{22}\text{Na}$  gamma (e)  $^{60}\text{Co}$  low (f)  $^{60}\text{Co}$  high. The red lines are linear fits to the data.

659 analysis.

660

TABLE IX. Systematic Effects of Drifting Peak Location

Radionuclide	Peak Energy	Fractional	Hourly Counts	Fractional Change
		Peak Shift	of Peak ROI	in Counts
$^{54}\text{Mn}$	835 keV (Det. 2)	$-2.4 \times 10^{-5}$	$3.01 \times 10^7$	$-6.4 \times 10^{-6}$
	835 keV (Det. 7)	$-5.6 \times 10^{-5}$	$3.58 \times 10^7$	$-1.33 \times 10^{-5}$
$^{22}\text{Na}$	511 keV	$-3.5 \times 10^{-5}$	$2.53 \times 10^7$	$-2.4 \times 10^{-6}$
	1275 keV	$2.25 \times 10^{-4}$	$4.2 \times 10^6$	$-1.089 \times 10^{-4}$
$^{60}\text{Co}$	1173 keV	$-1.8 \times 10^{-5}$	$1.36 \times 10^7$	$-3.07 \times 10^{-5}$
	1333 keV	$-2.43 \times 10^{-4}$	$1.13 \times 10^7$	$-9.86 \times 10^{-5}$

<sup>661</sup>      **ACKNOWLEDGMENTS**

<sup>662</sup>      We wish to thank J. J. Coy, R. de Meijer, S. Fancher, J. Herczeg, G. W. Hitt, J. H. Jenkins,  
<sup>663</sup> D. Koltick, M. Pattermann, P.A. Sturrock, and T. Ward for helpful communications. We  
<sup>664</sup> are deeply indebted to the staff of Oak Ridge National Laboratory for their assistance in  
<sup>665</sup> carrying out this experiment. This study was funded by the Office of Nuclear Energy, U.S.  
<sup>666</sup> Department of Energy under contract number DE-DT0004091.001b.

667      **REFERENCES**

---

- 668 [1] E. D. Falkenberg, *Apeiron* **8**, 32 (2001).
- 669 [2] D. Alburger, G. Harbottle, and E. Norton, *Earth and Planetary Science Letters* **78**, 168  
670        (1986).
- 671 [3] H. Siegert, H. Schrader, and U. Schötzig, *Applied radiation and isotopes* **49**, 1397 (1998).
- 672 [4] E. Fischbach, J. Buncher, J. Gruenwald, J. Jenkins, D. Krause, J. Mattes, and J. Newport,  
673        *Space Science Reviews* **145**, 285 (2009).
- 674 [5] J. H. Jenkins, E. Fischbach, J. B. Buncher, J. T. Gruenwald, D. E. Krause, and J. J. Mattes,  
675        *Astroparticle Physics* **32**, 42 (2009).
- 676 [6] S. E. Shnoll, T. A. Zenchenko, K. Zenchenko, E. Pozharskii, V. Kolombet, and A. A. Kon-  
677        radow, *Physics-Uspekhi* **43**, 205 (2000).
- 678 [7] Y. A. Baurov, A. Konradov, V. Kushniruk, E. Kuznetsov, Y. G. Sobolev, Y. V. Ryabov,  
679        A. Senkevich, and S. Zadorozsny, *Modern Physics Letters A* **16**, 2089 (2001).
- 680 [8] K. J. Ellis, *Physics in Medicine and Biology* **35**, 1079 (1990).
- 681 [9] D. Javorsek, P. Sturrock, J. Buncher, E. Fischbach, T. Gruenwald, A. Hoft, T. Horan, J. Jenk-  
682        ins, J. Kerford, R. Lee, J. Mattis, D. Morris, R. Mudry, J. Newport, M. Petrelli, M. Silver,  
683        C. Stewart, B. Terry, and H. Willenberg, in *AIP Conference Proceedings CP1182*, 1 (2009)  
684        p. 292.
- 685 [10] E. Fischbach, J. H. Jenkins, J. Buncher, J. T. Gruenwald, P. Sturrock, and D. Javorsek, in  
686        *Proceedings of the Fifth Meeting on CPT and Lorentz Symmetry* (World Scientific: Singapore,  
687        2011) pp. 168–173.
- 688 [11] D. Javorsek, P. Sturrock, R. Lasenby, A. Lasenby, J. Buncher, E. Fischbach, J. Gruenwald,  
689        A. Hoft, T. Horan, J. Jenkins, J. Kerford, R. Lee, A. Longman, J. Mattes, B. Morreale,  
690        D. Morris, R. Mudry, J. Newport, D. O’Keefe, M. Petrelli, M. Silver, C. Stewart, and B. Terry,  
691        *Astroparticle Physics* **34**, 173 (2010).
- 692 [12] P. Sturrock, J. Buncher, E. Fischbach, J. Gruenwald, D. Javorsek, J. Jenkins, R. Lee, J. Mat-  
693        tes, and J. Newport, *Astroparticle Physics* **34**, 121 (2010).

- 694 [13] J. H. Jenkins, D. W. Mundy, and E. Fischbach, Nuclear Instruments and Methods in Physics  
 695 Research Section A **620**, 332 (2010).
- 696 [14] P. Sturrock, J. Buncher, E. Fischbach, J. Gruenwald, D. Javorsek II, J. Jenkins, R. Lee,  
 697 J. Mattes, and J. Newport, Solar Physics **267**, 251 (2010).
- 698 [15] P. A. Sturrock, J. B. Buncher, E. Fischbach, D. Javorsek, J. Jenkins, and J. Mattes, The  
 699 Astrophysical Journal **737**, 65 (2011).
- 700 [16] P. A. Sturrock, E. Fischbach, and J. Jenkins, Solar Physics **272**, 1 (2011).
- 701 [17] J. Jenkins, E. Fischbach, P. Sturrock, and D. Mundy, in *Gravitational Waves and Exper-*  
 702 *imental Gravity*, edited by E. Augé, J. Dumarchez, and J. Trần Thanh Vân (THE GIOI,  
 703 2011).
- 704 [18] J. H. Jenkins, K. R. Herminghuysen, T. E. Blue, E. Fischbach, D. Javorsek, A. C. Kauffman,  
 705 D. W. Mundy, P. A. Sturrock, and J. W. Talnagi, Astroparticle Physics **37**, 81 (2012).
- 706 [19] P. A. Sturrock, G. Steinitz, E. Fischbach, D. Javorsek II, and J. H. Jenkins, Astroparticle  
 707 Physics **36**, 18 (2012).
- 708 [20] J. H. Jenkins, E. Fischbach, D. Javorsek II, R. H. Lee, and P. A. Sturrock, Applied Radiation  
 709 and Isotopes **74**, 50 (2013).
- 710 [21] D. O'Keefe, B. L. Morreale, R. H. Lee, J. B. Buncher, J. Jenkins, E. Fischbach, T. Gruenwald,  
 711 D. Javorsek, and P. A. Sturrock, Astrophysics and Space Science **344**, 297 (2013).
- 712 [22] P. Sturrock, L. Bertello, E. Fischbach, D. Javorsek II, J. Jenkins, A. Kosovichev, and  
 713 A. Parkhomov, Astroparticle Physics **42**, 62 (2013).
- 714 [23] P. A. Sturrock, E. Fischbach, and J. Jenkins, The Astrophysical Journal **794**, 42 (2014).
- 715 [24] S. Bergeson, J. Peatross, and M. Ware, Phys. Lett. **767**, 171 (2017).
- 716 [25] K. Kossert and O. Nähle, Astroparticle Physics **69**, 18 (2015).
- 717 [26] S. Pommé *et al.*, Phys. Lett. B **761**, 281 (2016).
- 718 [27] P. A. Sturrock, G. Steinitz, and E. Fischbach, Astropart. Phys. **98**, 9 (2018).
- 719 [28] J. H. Jenkins and E. Fischbach, Astroparticle Physics **31**, 407 (2009).
- 720 [29] T. Mohsinally, S. Fancher, M. Czerny, E. Fischbach, J. Gruenwald, J. Heim, J. Jenkins,  
 721 J. Nistor, and D. O'Keefe, Astroparticle Physics **75**, 29 (2016).
- 722 [30] P. S. Cooper, Astroparticle Physics **31**, 267 (2009).
- 723 [31] E. B. Norman, E. Browne, H. A. Shugart, T. H. Joshi, and R. B. Firestone, Astroparticle  
 724 Physics **31**, 135 (2009).

- 725 [32] T. Semkow, D. Haines, S. Beach, B. Kilpatrick, A. Khan, and K. O'Brien, Physics Letters B  
726 **675**, 415 (2009).
- 727 [33] K. Kossert and O. J. Nähle, Astroparticle Physics **69**, 18 (2015).
- 728 [34] D. Krause, B. Rogers, E. Fischbach, J. Buncher, A. Ging, J. Jenkins, S. N. Longuski, JM,  
729 and P. Sturrock, Astroparticle Physics **36**, 51 (2012).
- 730 [35] R. M. Lindstrom, E. Fischbach, J. B. Buncher, G. L. Greene, J. H. Jenkins, D. E. Krause,  
731 J. J. Mattes, and A. Yue, Nucl. Inst. Meth. Phys. Res. A **644**, 93 (2010).
- 732 [36] R. M. Lindstrom, E. Fischbach, J. B. Buncher, J. H. Jenkins, and A. Yue, Nuclear Instruments  
733 and Methods in Physics Research Section A **659**, 269 (2011).
- 734 [37] A. Palazzo, Modern Physics Letters A **28**, 1330004 (2013).
- 735 [38] E. Fischbach, J. H. Jenkins, and P. A. Sturrock, in *Gravitational Waves and Experimental  
736 Gravity*, edited by E. Augé, J. Dumarchez, and J. Trần Thanh Vân (THE GIOI, 2011).
- 737 [39] R. de Meijer, M. Blaauw, and F. Smit, Applied Radiation and Isotopes **69**, 320 (2011).
- 738 [40] R. de Meijer and S. Steyn, arXiv preprint arXiv:1409.6969 (2014).
- 739 [41] G. F. Knoll, *Radiation Detection and Measurement*, 3rd ed. (John Wiley and Sons, 2000).
- 740 [42] J. Bahcall and W. Press, Astrophysical Journal **370**, 730 (1991).
- 741 [43] P. Sturrock, J. Buncher, E. Fischbach, J. Gruenwald, D. Javorsek II, J. Jenkins, R. Lee,  
742 J. Mattes, and J. Newport, Astropart. Phys. **34**, 121 (2010).
- 743 [44] Wikipedia, “Standard deviation — wikipedia, the free encyclopedia,” (2016), [Online; ac-  
744 cessed 7-June-2016].
- 745 [45] R. de Meijer *et al.*, arXiv preprint arXiv:1610.01332 (2016).
- 746 [46] A. G. Parkhomov, Journal of Modern Physics **2**, 1310 (2011).
- 747 [47] *Nuclides and Isotopes: Chart of the Nuclides*, 16th ed. (Lockheed Martin, 2002).
- 748 [48] P. Huber, Phys. Rev. C **84**, 024617 (2011).
- 749 [49] V. Barnes, D. Bernstein, C. Bryan, N. Cinko, G. Deichert, J. Gruenwald, J. Heim, H. Kaplan,  
750 R. LaZur, D. Neff, J. Nistor, N. Sahelijo, and E. Fischbach, arXiv preprint arXiv:1606.09325  
751 (2016).
- 752 [50] J. Ashenfelter *et al.*, Nuclear Instruments and Methods in Physics Research Section A: Accel-  
753 erators, Spectrometers, Detectors and Associated Equipment **806**, 401 (2016).